Experimental study of turbulent oscillatory boundary layers in an oscillating water tunnel

Jing Yuan[a], Ole. S. Madsen[b]

[a]*Department of Civil and Environmental Engineering, National University of Singapore, 1 Engineering Dr. 2, Block E1A 07-03, Singapore 117576*
[b]*R.M. Parsons Laboratory, Department of Civil and Environmental Engineering, Massachusetts Institute of Technology, 15 Vassar St, Room 48-317, Cambridge, MA 02139, U.S*

Abstract

A high-quality experimental study including a large number of tests which correspond to full-scale coastal boundary layer flows is conducted using an oscillating water tunnel for flow generations and a Particle Image Velocimetry system for velocity measurements. Tests are performed for sinusoidal, Stokes and forward-leaning waves over three fixed bottom roughness configurations, i.e. smooth, "sandpaper" and ceramic-marble bottoms. The experimental results suggest that the logarithmic profile can accurately represent the boundary layer flows in the very near-bottom region, so the log-profile fitting analysis can give highly accurate determinations of the theoretical bottom location and the bottom roughness. The first-harmonic velocities of both sinusoidal and nonlinear waves, as well as the second-harmonic velocities of nonlinear waves, exhibit similar patterns of vertical variation. Two dimensionless characteristic boundary layer thicknesses, the elevation of 1% velocity deficit and the elevation of maximum amplitude, are found to have power-law dependencies on the relative roughness for rough bottom tests. A weak boundary layer streaming embedded in nonlinear waves and a small

but meaningful third-harmonic velocity embedded in sinusoidal waves are observed. They can be only explained by the effect of a time-varying turbulent eddy viscosity. The measured period-averaged vertical velocities suggest the presence of Prandtl's secondary flows of the second kind in the test channel. Among the three methods to infer bottom shear stress from velocity measurements, the Reynolds stress method underestimates shear stress due to missed turbulent eddies, and the momentum integral method also significantly underestimates bottom shear stress for rough bottom tests due to secondary flows, so only the log-profile fitting method is considered to yield the correct estimate. The obtained bottom shear stresses are analyzed to give the maximum and the first three harmonics, and the results are used to validate some existing theoretical models.
Keywords: Turbulent oscillatory boundary layer, Oscillatory Water Tunnel, Bottom shear stress, Laboratory experiment

1. Introduction

In coastal regions, surface waves generate turbulent near-bottom flows which provide the driving forces for sediment transport. Following linear wave theory, wave boundary layers are usually approximated by bottom-parallel oscillations which are uniform in the wave direction, i.e. turbulent oscillatory boundary layers. The early analytical studies assumed a time-invariant turbulent eddy viscosity to solve the boundary layer equation, e.g. Kajiura (1968), Grant (1977) and Brevik (1981) for sinusoidal wave boundary layers, and Grant and Madsen (1979), Fredsøe (1984) and Sleath (1991) for combined wave-current boundary layers. Neglecting the temporal variation of

turbulent eddy viscosity is against the unsteady nature of oscillatory flows, so among others, Trowbridge and Madsen (1984a,b), Lavelle and Mofjeld (1983) and Gonzalez-Rodriguez and Madsen (2011) developed more elaborate models based on a time-varying turbulent eddy viscosity. Besides analytical models, numerical models based on various turbulent closure schemes also have been developed (e.g. Davies et al., 1988; Holmedal and Myrhaug, 2006; Scandura, 2007).

The development of theoretical models relies heavily on experimental studies. Dimensional analysis (e.g. Sleath, 1987) suggests that turbulent oscillatory boundary layers are controlled by two dimensionless parameters: the amplitude Reynolds number $Re{=}A_{bm}U_{bm}/\nu$ and the relative roughness A_{bm}/k_b, where U_{bm} is the near-bottom wave orbital velocity amplitude, A_{bm} is the near-bottom excursion amplitude, ν is the molecular kinematic viscosity of the fluid and k_b is the bottom roughness. For a surface wave which can induce noticeable amounts of sediment transport, A_{bm} and U_{bm} can reach the orders of 1m and 1m/s, respectively, so the corresponding Re and A_{bm}/k_b can be up to O(10^6) and O(10^3), respectively. Many previous experimental studies are performed in small-scale wave flumes (e.g. Kemp and Simons, 1982, 1983; Cox et al., 1996; Dixen et al., 2008) or shaking platforms (e.g. Krstic and Fernando, 2001; Hay et al., 2012a,b). However, the physical limitations of these facilities make it impossible to achieve the high values of Re and A_{bm}/k_b under prototype flow conditions. Thus, most full-scale experimental studies are conducted in another type of facility: oscillating water tunnels (OWT). These facilities are usually U-shaped tunnels. A piston located at one end of the tunnel produces oscillatory motions in the entire tunnel. As

pointed out by many researchers (e.g. van der Werf et al., 2009), OWT flows are approximations to those under progressive waves, since they are uniform along the longitudinal direction, i.e. $\partial u/\partial x = 0$. Thus, some boundary layer processes, e.g. the boundary layer streaming suggested by Longuet-Higgins (1953), are not present. Nevertheless, this drawback is offset by the OWT's ability to obtain highly-accurate experimental data at prototype scales. For simplicity, the oscillatory OWT flows will be referred to as waves hereafter. Jonsson (1963) followed by Jonsson and Carlsen (1976) conducted two sinusoidal-wave tests over artificially rippled bottoms in the very first OWT described by Lundgren and Sorensen (1957). After that, Sleath (1987) studied the characteristics of turbulence in oscillatory boundary layers in a relatively smaller OWT. Jensen et al. (1989) performed similar experiments to Sleath (1987) in a higher range of Re. These three studies only considered sinusoidal oscillatory flows, however, the nonlinearity of coastal waves makes the near-bottom flow skewed (peaked crest and flat trough) and asymmetric (forward-leaning crest). Very few experimental studies have been performed for such flow conditions. Ribberink and Al-Salem (1995) reported limited measurements of skewed oscillatory boundary layer flows as by-products of their experimental study of skewness-induced net sediment transport. Very recently, van der A et al. (2011) systematically studied asymmetric oscillatory boundary layers over rough bottoms.

Previous OWT studies provide valuable experimental results for understanding turbulent oscillatory boundary layers, but the work is still not finished. A significant problem is the experimental determination of bottom shear stress. As will be introduced in Section 5, bottom shear stress is

generally inferred from velocity measurements via three methods: the log-profile fitting method, the momentum integral method and the Reynolds stress method. Ideally, they should give identical estimates. However, Sleath (1987) showed that the observed Reynolds stress was significantly smaller than the shear stress given by the momentum integral method. A less significant but still noticeable discrepancy was observed by van der A et al. (2011). They also showed that the momentum integral method gave bottom shear stresses which are 30%$\sim$50% smaller than those from the log-profile fitting method. Similar discrepancies are observed in experimental studies using other types of facilities, such as the shaking platform experiments by Hay et al. (2012b). Thus, the three methods generally give bottom shear stress in the sequence: Reynolds stress<momentum integral<log-profile fitting. It is unknown which method yields the correct estimate, so researchers face the problem of having to choose the "right" measurements for model validations, e.g. Abreu et al. (2013) chose the results from the momentum integral method which is argued invalid by van der A et al. (2011). Another unsettled issue is the quantification of bottom roughness which is an important input parameter for most theoretical models. The seminal work by Nikuradse (1932, 1933) provides a quantitative understanding of bottom roughness for steady turbulent boundary layers, but whether his findings are applicable for unsteady flows must be confirmed through a systematic experimental study which is comparable to Nikuradse's work. Previous OWT studies did not pay much attention to bottom roughness, so a detailed experimental effort devoted to clarification of this issue is desirable.

In this study, we conduct full-scale experiments using an newly-built

OWT (see Yuan et al. (2012) for a detailed description) for flow generation and a state-of-the-art Particle Image Velocimetry (PIV) system for velocity measurements. Tests are performed for three types of periodic oscillatory flows over three different fixed bottom roughness configurations. Several flow conditions are covered for each combination of flow type and bottom roughness configuration, so the number of tests are sufficiently large to ensure the reliability of the obtained conclusions. The experimental setup is introduced in Section 2. The experimental determination of bottom roughness will be discussed in Section 3. Some characteristics of turbulent oscillatory boundary layers will be presented in Section 4. The experimental determination of bottom shear stress will be addressed in Section 5.

2. Experimental setup

2.1. Experimental facility

The experimental facility is a newly-built OWT, named the Wave-Current-Sediment facility (WCS), in the Hydraulic Engineering Laboratory of the Department of Civil and Environmental Engineering at the National University of Singapore, as shown in Fig. 1. The main part is a 10m-long, 50cm-deep and 40cm-wide horizontal test channel with glass sidewalls and acrylic lids along its entire length. Below the 50cm working depth, a 20cm-deep trough for holding sediments is currently fitted with wooden false bottom blocks which can serve as the foundation to mount bottom roughness plates. The transparency of sidewalls and lids makes it very convenient to set up any experimental apparatus which requires introducing light or laser beams into the channel. Two stainless steel vertical cylindrical risers of 1m-diameter

are connected to the test channel through honeycomb filters to make in- and outflows uniform. One riser is open to the atmosphere and the other contains a programmable, hydraulically actuated piston which can generate a variety of periodic or irregular oscillations. The maximum excursion amplitude of the piston is 500mm which corresponds to roughly 2m maximum excursion amplitude of flows in the 40cm-by-50cm test section. Limited by the 40kN maximum driving force of the piston, the maximum amplitudes of piston velocity and acceleration are 500mm/s and 500mm/s^2 for periods 2s$<T<$12s, so the corresponding maximum amplitudes of flow velocity and acceleration in the test section are about 2m/s and 2m/s^2. The entire structure is supported by a pivot and a hydraulic jack, so it can be tilted (up to 1/20) to include the bottom slope effect into our physical modeling. A current generation system has been built to superimpose a current on oscillatory flows. The core part is a Börger EL1550 Rotary Lobe pump placed in the basement underneath the WCS. It can produce a current of up to 60cm/s average velocity in the test section. One significant feature of this pump is that it can maintain a steady discharge even when the pressure difference across the pump changes in time, e.g. due to wave generation. Moreover, the direction of the current can be easily reversed by reversing the pump's rotation. A sediment trap tank is inserted in the pipe system to capture suspended sediments when performing experiments with significant suspended sediment transport. The current enters or leaves the main test section through flexible telescoping pipe connections, allowing tilting the entire facility with the current generation system operating. With all these features, the facility is able to model most important physical processes of oscillatory boundary layers in coastal

regions.

2.2. PIV measurements

Velocity measurements are obtained using a 2-dimensional PIV system supplied by the TSI Corporation. The flow is seeded with nearly neutrally-buoyant silver-coated seeding particles with diameter of $10\mu m$. To illuminate the near-bottom flow field, a double-pulsed YAG 135-15 Litron Nano L laser produces a thin laser sheet which is introduced into the test channel vertically downward through the transparent lid. Since the primary flow is in the longitudinal direction, the laser sheet is carefully aligned with the lateral center line of the test channel to remove sidewall effects. It is also located close to the longitudinal center of the test channel, so the end effect is reduced to a minimum. For each sampling, two images of the illuminated area are captured using a high-speed Powerview 4M Plus 2000-by-2000 pixels camera with a very short time interval Δt. The firing of laser and the image capture by the camera is controlled and synchronized by a 610035 LaserPulse Synchronizer. For most tests in this study, the camera is about 70cm from the target flow field and uses a lens with fixed 105mm focal length, which gives a resolution parameter λ=50μm/pixel. This corresponds to a roughly 10cm-by-10cm captured area. For some tests with over 10cm thick boundary layers, another lens with 50mm focal length is used to double the size of the captured area. By performing cross-correlation analysis of the image pair of a single sampling using the Insight 4G software supported by TSI, the displacements and hence the velocities of seeding particles are obtained. Insight 4G first divides the digital image into rectangular interrogation grids, and then performs cross-correlation analysis for each grid to get velocities. Since the

horizontal component of velocity is the dominant one, the interrogation grid is stretched to 128 (horizontal)-by-16 (vertical) pixels. The analysis gives velocity vectors in each quadrant of an interrogation grid, so the spacing of the velocity measurements is roughly 3.2mm-by-0.4mm, which is fine enough to reveal most important details of turbulent oscillatory boundary layers. The time interval Δt between the image pair of a single PIV measurement is determined by requiring that the maximum Reynolds-average flow velocity U_{max} gives a particle displacement less than 16 pixels, i.e. $\Delta t{=}16 \cdot \lambda / U_{max}$. The PIV sampling rate is 5.12Hz for all tests.

To increase the PIV's accuracy, the image background brightness is removed from all images, and the grids containing solid bottom elements are also masked off. Thus, only 1$\sim$3% of the obtained velocity vectors are erroneous due to imperfect flow seeding or analysis error. Since the erroneous vectors are quite few, they are simply replaced by their local mean vectors based on its neighboring 8 vectors. The obtained velocity fields over N wave periods are phase-averaged into a single period T:

$$\hat{\psi}(x,z,t) = \frac{1}{N}\sum_{n=1}^{N} \psi(x,z,t+(n-1)T), 0<t<T \qquad (1)$$

where ψ is either the horizontal or vertical component of flow velocity (u,w), t is the time, and (x,z) are the horizontal and vertical coordinates. If the scale of individual bottom roughness is much smaller than the scale of the interrogation grid, the measurements at the same vertical level but different longitudinal positions are effectively homogeneous. Therefore, we can perform a spatial average to consolidate the 2D velocity field which has M

columns into a vertical velocity profile:

$$< \psi(z,t) >= \frac{1}{M}\sum_{m=1}^{M}\psi(x_m,z,t) \tag{2}$$

The Reynolds-averaged quantities are obtained by performing both spatial and phase average:

$$\begin{aligned} &< \hat{\psi} > (z,t) = \\ &\frac{1}{MN}\sum_{m=1}^{M}\sum_{n=1}^{N}\psi(x_m,z,t+(n-1)T), 0<t<T \end{aligned} \tag{3}$$

The associated turbulent fluctuation is then given by:

$$\psi'(x,z,t) = \psi(x,z,t) - < \hat{\psi} > (z,t) \tag{4}$$

The Reynolds stress normalized by fluid density is obtained through the double average:

$$< -u'w' > (z,t) = \frac{1}{MN}\sum_{m=1}^{M}\sum_{n=1}^{N}u'w' \tag{5}$$

It should be noticed that the turbulent fluctuation, as defined by Eq. (4), will include fluctuations due to spatial inhomogeneity. Therefore, the Reynolds stress given by Eq. (5) is an equivalent Reynolds stress which contains the correlation of the spatial fluctuations of u and w. This is essentially the form drag due to individual roughness elements. In the following part of this paper, unless otherwise indicated, we will for simplicity use $\psi(z,t)$ to denote the double-averaged quantities.

2.3. Bottom conditions

In this study, three bottom conditions, a smooth bottom and two rough bottoms, are included. The smooth bottom is formed by 10 pieces of 8mm-thick, 40cm-wide and 1m-long flat aluminum plates mounted on the wooden

false bottom and painted black to reduce laser reflection effects. For the two rough bottoms, bottom roughness elements are fixed to exclude the movable bottom effect. One rough bottom, as shown in Fig. 2a, is built by gluing 3M^{TM} 710 Safety-WalkTM Slip-Resistant Coarse tapes onto the aluminum plates. These rough tapes consist of large abrasive particles bonded by a tough, durable polymer to a plastic film, so they to some extent resemble sandpaper. For simplicity, this bottom will be referred to as the "sandpaper" bottom hereafter. To estimate the horizontal and vertical scales of bottom roughness elements, L_x and D, a side-view image of an 18cm-long cut through the "sandpaper" was taken. A small part of this image is shown in Fig. 2c. By searching for the border between the gray image background and the black bottom, a profile which shows the waviness of the bottom surface is obtained. The wave-length spectrum of this bottom profile suggests that the average wave length L_r is 2.6mm and the root-mean-square wave height H_r is 0.62mm, so the undulation of the rough surface is relatively mild. The other rough bottom is the ceramic-marble covered bottom shown in Fig. 2(b,d). A mono-layer of 12.5mm-diameter ceramic marbles are carefully placed and glued onto the aluminum plates, so this bottom has a much larger roughness than the "sandpaper" bottom. Using such uniform roughness elements avoids the randomness of the "sandpaper" bottom, so the bottom condition is well-defined, e.g. providing an origin for a vertical coordinate as the top of the ceramic marbles, and the experimental results will be ideally suited for scientific understanding of the fluid-solid interactions.

2.4. Flow conditions

Three periodic wave shapes, sinusoidal, Stokes and forward-leaning waves, are included in this study. The latter two are the sum of two harmonics:

$$u_\infty(t) = U_{\infty,1}\cos(\omega t) + \frac{U_{\infty,1}}{4}\cos(2\omega t + \varphi_{\infty,2}) \tag{6}$$

The second-harmonic phase $\varphi_{\infty,2}$ is 0° for Stokes waves and 90° for forward-leaning waves. As shown in Fig. 3, they represent the skewness and the asymmetry of near-bottom flows under nonlinear waves. For each wave shape, a variety of wave amplitudes and two wave periods (6.25s and 12.5s) are considered, as summarized in Table 1. Here the amplitudes are controlled by the first-harmonic displacement amplitude of the piston a_1, so the measured $U_{\infty,1}$ may deviate slightly (1∼5%) from the target values listed in the fourth column of Table 1 which are actually the cross-section averaged $U_{\infty,1}$ based on a_1 (first-harmonic amplitude of piston displacement). The PIV sampling frequency is 5.12Hz for all tests, so the number of samplings per period is 32 for the short-period (6.25s) tests and 64 for the long-period (12.5s) tests. Preliminary tests were performed with increasing numbers of wave periods, i.e. 16, 32 and 64. Experimental results suggest that there is virtually no difference between the Reynolds-averaged measurements (Eq. (3) and (5)) given by the 32-period and 64-period tests, so all tests are sampled for 32 wave periods.

To test whether the WCS can precisely generate a specified oscillatory motion, a preliminary Stokes-wave test ST400a over the smooth wooden false bottom was conducted. The piston displacement was recorded, and two PIV measurements located symmetrically on both sides of the lateral

centerline, i.e. half-width distance (20cm) apart, were performed. Based on the conservation of total volume, the measured piston displacements can be used to give the cross-section average velocity U_{piston} which should be identical to the target cross-section average velocity U_{target} based on the intended piston displacements. Since the smooth turbulent boundary layer is very thin, these two velocities should be very close to the two measured free-stream velocities $U_{PIV,1}$ and $U_{PIV,2}$. The comparisons are based on the amplitudes of the first three harmonics, $U_{\infty,1}$, $U_{\infty,2}$ and $U_{\infty,3}$, and the second-harmonic phase lead $\varphi_{\infty,2}$, as shown in Table 2. $U_{\infty,1}$ and $U_{\infty,2}$ of U_{piston} deviate from those of U_{target} by only 0.4cm/s and 0.02cm/s, respectively. Meanwhile, $\varphi_{\infty,2}$ of U_{piston} deviates from the target value by only about 5°. If necessary, this slight error in phase can be corrected by changing the phase of the input signal, i.e. use $\varphi_{\infty,2}$=5.42°. The measured $U_{\infty,3}$ of U_{piston}, as well as other unintended higher order harmonics, is negligibly small. Thus, U_{piston} agrees very well with U_{target}, indicating that the system can accurately produce a specified piston motion. The difference between U_{piston}, $U_{PIV,1}$ and $U_{PIV,2}$ is also immaterial. The relative discrepancies among amplitudes are of O(1%), and the discrepancy among second-harmonic phases $\varphi_{\infty,2}$ is less than 1°. These results show that the flow is laterally uniform, responds accurately to the target piston movement and demonstrate that the WCS has excellent wave generation capabilities.

A two-part scheme, "Flow_Bottom", is used to identify tests. The first part indicates the flow conditions. For oscillatory flows, it is chosen from the test ID listed in Table 1. Some pure current tests were also performed in this study. Current generation is specified by the pump's working frequencies f,

and the cross-section average velocity $\bar{u}$ can be roughly estimated as:

$$\bar{u}[cm/s] = f[Hz], \quad 13Hz < f < 50Hz \tag{7}$$

Thus, currents are simply named in the form of "C" plus a number indicating f, e.g. "C13" is a pure current test with a 13Hz pump frequency. The second part of the test IDs is the bottom identifier which is chosen from "sm" (the smooth bottom), "sa" (the "sandpaper" bottom) and "ce" (the ceramic-marble bottom). For example, the test ST400a_ce is the Stokes-wave test given by the fifth row in Table 1 over the ceramic-marble bottom and test C40_sa denotes a test with a pure current of ∼40cm/s mean velocity over the "sandpaper" bottom.

3. Theoretical bottom location and bottom roughness

Steady turbulent boundary layers follow the law of the wall in the near-bottom region:

$$u = \frac{u_*}{\kappa} \ln(\frac{z}{z_0}) \tag{8}$$

where z_0 is a roughness scale, u_* is the shear velocity, $\sqrt{\tau_b/\rho}$, with τ_b being the bottom shear stress, and κ is the von Kármán constant which is found to vary between 0.38∼0.42 in various studies (we simply use 0.40 hereafter). A bottom roughness is customarily defined as k_b=30z_0. For oscillatory turbulent boundary layers, many experimental studies, e.g. Jensen et al. (1989), show that the law of the wall is also applicable. Since the vertical coordinate z is a variable in Eq. (8), the theoretical bottom location z=0 must be experimentally determined together with k_b.

3.1. Theoretical bottom location

3.1.1. Smooth bottom tests

As shown in Fig. 4a, where the laser sheet hits the smooth bottom surface, the strong laser reflection makes the local brightness exceed the maximum acceptable brightness of the PIV camera, which is indicated by the pink layer. The intensity of the laser sheet decays towards its edges, producing a bell-shaped distribution of brightness across the pink layer. For the smooth bottom z=0 is where the brightness reaches its maximum, and consequently can be obtained by fitting a normal distribution:

$$B(X,Z) = \frac{1}{\sigma(X)\sqrt{2\pi}} e^{-\frac{(Z-Z_0(X))^2}{2\sigma(X)^2}} \tag{9}$$

where B is the PIV image's brightness (0 to 4095), (X, Z) are the horizontal and vertical image coordinates (in pixels) with the origin set at the lower-left corner of the image, σ is the standard deviation of the normal distribution and Z_0 is the vertical coordinate of the distribution's peak. To remove image noises, every 50 adjacent single-pixel profiles are averaged to give a relatively smooth 50-pixel-averaged brightness profile, as shown in Fig. 5. The fitting is based on data points within 2σ from the peak of the fitted distribution, and the points inside the flat region (B=4095) around the peak are excluded since they are not actual measurements. The fitted curve in Fig. 5 nicely passes through the selected data points and the obtained Z_0 is roughly located at the center of the flat region with a mere 0.2-pixel 95%-confidence interval. As shown in Fig. 6a, the obtained bottom profile $Z_0(X)$ can be reasonably approximated by a straight line with a roughly 1/900 slope due to imperfect camera alignment. We simply neglect this very small slope and take the

average over the horizontal span as the bottom surface level. The maximum introduced error which occurs at both ends will be only 1 pixel (0.05mm). Another determination error is due to the deflection of the glass sidewalls under oscillating water pressure, which affects the refraction of laser beams as they travel across the sidewalls and therefore makes the image of the bottom oscillate. Fig. 6b shows the period variation of Z_0 obtained at a fixed horizontal location X=1025 for test SP400a_sm. This variation can be approximated by a sinusoidal temporal variation with roughly 1-pixel amplitude. Since test SP400a_sm is very close to the design limit of the WCS, the determination error due to sidewall deflection should be less than 1 pixel. The final z=0 is obtained by averaging the bottom profiles over a wave period and over the horizontal span, so the accumulated error is no more than 2 pixels (0.1mm). Thus, the theoretical bottom location for the smooth bottom is determined with extreme accuracy.

3.1.2. Rough bottom tests

For the two rough bottoms, a temporary vertical coordinate y is defined as follows. For the ceramic-marble bottom, y=0 is the mean crest level visually determined from PIV images by drawing a horizontal line across all observed crests, as indicated by the dashed yellow line in Fig. 4b. For the "sandpaper" bottom, such a visual determination of the crest level is not accurate enough, so the methodology to give $Z_0(X)$ for the smooth bottom is applied to get a "bottom profile", as indicated by the black wavy line in Fig. 4c. This "bottom profile" has a representative wave height 0.34mm and a representative wave length (2.1mm) which are smaller than the values obtained in Section 2.3. The reason is that the bottom regions of elements are

blocked by the elements in front of them, so only top regions are detected. The level of the "top" of the "sandpaper" bottom, y=0, is defined as the mean level inferred from laser measurements plus half of H_r=0.34mm, which gives the yellow dashed line in Fig. 4c. The vertical coordinate z is related to y by z=y+Δ, where Δ is a zero offset. Thus, the determination of z=0 is equivalent to the determination of Δ. Different values of Δ are tried in the log-profile fitting to determine an optimal value which gives the coefficient of determination R^2 closest to unity in the log-profile fitting. The Reynolds-averaged velocity profiles of pure current tests and the first-harmonic velocity amplitude profiles of sinusoidal wave tests are used for this analysis.

Since measurements in the immediate vicinity of the bottom are invalid due to locally large amount of bad PIV measurements, a lower limit for data selection requires that the percentage of good vectors at a certain vertical level must exceed 75%. Usually, it gives a lower limit between y=0.5mm and y=1.5mm. At these levels, measurements suggest that the local streamwise variation of velocity is less than 2% of the mean value, so the effect of individual roughness elements is insignificant. To avoid using data within the viscous sublayer or buffer layer, the thickness of buffer layer (Jiménez, 2004) is applied as another lower limit:

$$y + \Delta > \frac{100\nu}{u_*} \tag{10}$$

The overall lower limit for data selection is the higher of Eq. (10) and the 75%-good-vector threshold. For turbulent sinusoidal wave boundary layers, Grant (1977) shows that the log-profile approximation is only good in the region where the normalized vertical coordinate $\xi = z/l$ is very small, where

l is a characteristic boundary layer length scale defined as:

$$l = \frac{\kappa u_{*w}}{\omega} \tag{11}$$

with u_{*w} being the maximum wave shear velocity, which is approximately obtained from fitting the first-harmonic velocity amplitude profile. To have enough (5$\sim$10) data points, ξ=0.15 is chosen as the upper limit for data selection in this study. For pure current boundary layers, the logarithmic approximation is valid for small values of $(y + \Delta)/\delta_c$, where δ_c (always over 10cm in this study) is the boundary layer thickness. Thus, we simply take y=1cm as the upper limit for data selection, since this ensures that $(y+\Delta)/\delta_c$ is less than 0.1 and still can give 20-25 data points which is sufficient for log-profile fitting.

Fig. 7a shows the variation of 1-R^2 as a function of Δ for log-profile fitting of tests over the ceramic-marble bottom. Some curves are not continuous because the number of selected data points change with Δ, but this does not affect the general variation of the curves. All the six tests have quite well-defined minimum values of 1-R^2 of O(10^{-5}) to O(10^{-4}). The obtained values of optimal Δ are shown in the top half of Table 3. The average value based on the four wave tests, 3.95mm, is in excellent agreement with the one obtained from the two current tests, 4.05mm. Given the widely-accepted validity of using log-profile fitting to get Δ for steady turbulent flows, this agreement demonstrates that the same analysis based on the first-harmonic velocity amplitude profiles is also valid for oscillatory flows. In addition, this indicates that the data selection rules, especially the upper limit for wave tests, ξ_{max}=0.15, are appropriate. The average Δ based on all the six tests is 4.0mm, which is equal to 32% (1/3) of the diameter of

ceramic marbles (D=12.5mm). This is in good agreement with the Δ=0.35D reported by Bayazit (1976) who studied steady turbulent boundary layers in an open flume using uniform fixed hemispheres as bottom roughness. The standard deviation among obtained Δ is 0.4mm, which is only 10% of the mean value, so the determination of the theoretical bottom location for the ceramic-marble bottom is very accurate.

Fig. 7b shows the variation of 1-R^2 as a function of Δ for the "sandpaper" bottom. Test SP200_sa has the thinnest boundary layer, so only 5 data points meet the rules for data selection. Thus, this test suffers the largest determination error for Δ. Test C13_sa has a roughly 10mm lower limit for data selection (Eq. (10)), so the somewhat arbitrarily chosen upper limit (z<10mm) must be relaxed to give a sufficient number of data points. However, these data points have large values of y (>10mm), which makes 1-R^2 very insensitive to adding a small Δ. For these reasons, both tests do not give a minimum within the acceptable range of Δ, i.e. between 0$\sim$1mm, and are therefore not included in the statistics for Δ. It should be noted that these two tests are still included in later analyses using the Δ value obtained from other tests. To have at least two current tests, C13_sa is replaced by another test, C45_sa. As can be obtained from the bottom half of Table 3, the average Δ is 0.60mm for the three wave tests and 0.61mm for the two current tests, so the wave tests and the current tests are controlled by the same Δ, in agreement with our finding for the ceramic-marble bottom. The five tests give an overall average Δ=0.60mm and a standard deviation of only 0.1mm, so the experimental determination is very accurate.

3.2. Bottom roughness

Log-profile fitting is re-performed with the determined z=0 to obtain experimental values of bottom roughness.

3.2.1. k_b of the smooth bottom

The near-bottom parts of measured velocity profiles and fitted logarithmic profiles of two typical smooth bottom tests, a current test C40_sm and a wave test SP400a_sm, are shown in Fig. 8. For easy comparisons, u and z are normalized as follows:

$$\phi = \frac{u}{u_*},\ \eta = \frac{z}{\nu/u_*} \tag{12}$$

The selected data points all nicely collapse onto the fitted straight lines, which confirms the existence of a near-bottom logarithmic layer. The measured current velocity profiles of test C40_sm, Fig. 8a, begins to deviate from the fitted straight lines at about η=100, which proves the existence of the buffer layer and the correctness of using Eq. (10) as one of the lower limits for data selection. Since the wave boundary layer is very thin, only 5 points can be selected for the wave test SP400a_sm shown in Fig. 8b. Nevertheless, a few points above the upper limit (the upper red cross) still reasonably fall on the fitted logarithmic profiles, indicating the upper limit is conservatively defined. The results of the log-profile fittings are shown in Table 4. The confidence level for u_* is given by a normalized 95%-confidence interval $\Delta u_*/u_*$, and the confidence level for k_b is indicated by a 95%-confident factor $r_{\Delta k} \geq 1$, i.e. the true k_b is 95%-likely between $k_b/r_{\Delta k}$ and $k_b \cdot r_{\Delta k}$. The values of 1-R^2 are of O(10^{-5}) to O(10^{-4}), suggesting very good properties of log-profile fittings.

Generally speaking, $\Delta u_*/u_*$ is of the order 1%, and $r_{\Delta k}$ is less than 1.1. Therefore, both k_b and u_* are obtained with excellent accuracy.

For steady smooth turbulent boundary layer flows, the classic experimental study of Nikuradse (1932) suggests that the near-bottom logarithmic layer is controlled by an effective bottom roughness $k_{b,p}$:

$$k_{b,p} = \frac{3.3\nu}{u_*} \tag{13}$$

With the fitted values of u_*, this equation gives the predictions for $k_{b,p}$ shown in Table 4. For the current tests, the ratio $k_{b,p}/k_b$ has a 0.96 average and a 0.07 standard deviation, which demonstrates the validity of Eq. (13) and also verifies the accuracy of our measurements. For the wave tests, the values of $k_{b,p}/k_b$, 0.83±0.04, are remarkably consistent. Given the fact that the 95%-confidence factor of k_b can be up to 1.37, and only three tests are available, this consistency may be just a coincidence. In fact, if adding one or two data points outside the ranges of our data selection limits, this ratio can vary between 0.6 and 1.0. Nevertheless, the fitted roughness is always larger than the predicted roughness. According to Grant (1977), the u_* given by fitting the amplitude profile of first-harmonic velocity is approximately the maximum shear velocity related to the maximum bottom shear stress. It may make more sense to predict $k_{b,p}$ from Eq. (13) using a period-averaged u_* which is smaller than the maximum shear velocity. For example:

$$\bar{u}_* = \frac{1}{T}\int_0^T \sqrt{|\frac{\tau_b(t)}{\rho}|}dt \tag{14}$$

If the bottom shear stress is assumed to follow a sinusoidal temporal variation, $\bar{u}_*$ given by Eq. (14) is 76% of the maximum shear velocity, so using

it in Eq. (13) nicely removes the differences between $k_{b,p}$ and k_b, resulting in $k_{b,p}/k_b$=1.09±0.05. Given the limited number of tests and the relatively large experimental uncertainty, this study cannot conclusively support the correctness of adopting Eq. (14), as the definition of $\bar{u}_*$ in Eq. (13). Nevertheless, it is reasonable to conclude that a period-averaged shear velocity $\bar{u}_*$ which is smaller than the maximum u_* should be used in Nikuradse's empirical formula (Eq. (13)) to give the effective bottom roughness for oscillatory smooth turbulent boundary layer flows. We tentatively propose the definition of $\bar{u}_*$ given by Eq. (14), but future experimental investigations are required to estimate its accuracy.

3.2.2. k_b of rough bottoms

Nikuradse's (1933) rough-pipe experiments show that for rough turbulent boundary layer flows k_b depends on a roughness Reynolds number defined as:

$$Re_* = \frac{k_N u_*}{\nu} \tag{15}$$

where k_N is the Nikuradse equivalent sand grain roughness. In the fully rough turbulent regime where Re_* is sufficiently high, k_b is always equal to k_N, which also defines k_N. It should be noted that for bottoms consisting of densely packed sand-grain-shaped 3D roughness elements of diameter d, e.g. the inner surface of Nikuradse's pipes, k_N should equal d, but for other bottom roughness configurations, e.g. ripples, k_N may not be equal to the physical scale of the bottom roughness elements. When Re_* is less than 70∼100, k_b varies with Re_* in a manner described by:

$$\frac{k_b}{k_N} = 30e^{-\kappa C(Re_*)} \tag{16}$$

Nikuradse obtained the experimental determination of $C(Re_*)$ shown in Fig. 9 from his sand grain roughness experiments. When Re_* is less than 3$\sim$5, the flow enters the smooth turbulent regime, so C varies linearly with $\ln(Re_*)$. This curve of $C(Re_*)$ is usually assumed applicable for any rough bottom.

Fig. 10 shows the measured velocity profiles and the fitted logarithmic profiles for four representative tests (two currents and two waves) over the two rough bottoms. Similar to the tests over the smooth bottom, the selected data points tightly follow the fitted logarithmic profiles. The results of the log-profile fittings are shown in Table 5 and Table 6. The three parameters, 1-R^2, $\Delta u_*/u_*$ and $r_{\Delta k}$ are as "good" as those for smooth bottom tests, indicating equally good qualities of log-profile fittings. Because of the uncertainty associated with few data points, tests SP200_sa and C13_sa are worse than the rest, and they are also the two tests that did not give acceptable values for zero offset Δ.

For the tests over the "sandpaper" bottom shown in Table 5, k_b clearly increases with u_* from test C13_sa to test SP250_sa. The two strongest tests, SP400a_sa and SP250_sa, have nearly identical k_b, 3.60mm and 3.77mm, indicating that they are in the fully rough turbulent regime. Thus, k_N for the "sandpaper" bottom is taken as the their average, k_N=3.69mm. The roughness Reynolds number Re_* is calculated for each test with this k_N and the fitted u_*. The corresponding values of $C(Re_*)$ are inferred from k_b as follows:

$$C = -\ln(\frac{k_b}{30k_N})/\kappa \tag{17}$$

The experimental results are compared with those of Nikuradse (1933) in

Fig. 9. The present study does not cover the very low Re_* region, but in the remaining region the general patterns of variation are similar. However, clear differences between the two studies are observed. First, the beginning of the fully rough turbulent regime is delayed to Re_* =300$\sim$400 for the "sandpaper" bottom. Second, the maximum C in the transition regime is over 12.5, and could be even larger as Re_* further decreases, so it is considerably larger than the C_{max}=9.6 obtained by Nikuradse, which means the effect of flow conditions on k_b is more significant. These results indicate that the present "sandpaper" bottom does not behave in the same manner as the rough boundary made of densely-packed sand grains in Nikuradse's study. This is possibly because k_b also depends on the horizontal geometries of bottom roughness elements and their spacing, which are not considered in Eq. (17). As illustrated in Fig. 11a, for the present sandpaper bottom individual sand grains are loosely placed and coated with a layer of a black rubberized substance. The vertical scale is roughly 1/4 of the horizontal scale, as discussed in Section 2.3, so individual elements have much larger lee space than the densely-packed sand grains in Nikuradse's study (Fig. 11b). Therefore, the flow separation can even reach the bottom region of roughness elements, and consequently the area on the lee side with low pressure is relatively larger and the flow resistance is higher, which is reflected in larger bottom roughness. This explains why k_N for the sandpaper bottom is almost 6 times the estimated physical scale of the bottom roughness H_r=0.62mm. The rubberized substance coating of the "sandpaper" makes the surface of bottom roughness elements less angular, which may increase the required Re_* to get fully developed eddies, so the beginning of fully rough turbulent regime

is delayed. The observed discrepancies indicate that the curve of C versus Re_* given by Nikuradse is not universally applicable. For bottoms which are not similar to his packed-sand-grain bottom, $C(Re_*)$ must be re-determined experimentally.

For the tests over the ceramic-marble bottom shown in Table 6, the fitted bottom roughness has little variability, i.e. between 15.70mm and 22.95mm, indicating that all tests are in the fully rough turbulent regime. The average k_N is 20.0mm, and the associated standard deviation is only 3mm or 15% of the average. With k_N=20mm, the lowest value of Re_* is over 300, which confirms that all tests are in the fully rough turbulent regime. Since the ceramic marbles are densely packed and their surfaces are much smoother than angular real sand grains, it is expected that the k_N should be equal to or smaller than D. However, we obtain k_N=20mm which is 1.6 times the diameter of the ceramic marbles (12.5mm). The reason for obtaining a larger k_N is likely to be the anisotropy of bottom resistance. As shown in Fig. 12, the bottom is built by triangular packing of uniform ceramic marbles. If the flow is along a side of the equilateral triangle, e.g. the green arrow, some streamlines can pass through the valleys formed by two rows of ceramic marbles without much blockage, so the local flow feels only a very small resistance. However, if the flow direction is perpendicular to any side of the equilateral triangles, e.g. the red arrow, all streamlines have to rise up to climb over the blockage and separate from the surface shortly after the crest, so the flow feels more resistance, and consequently the bottom roughness for the second scenario is larger than for the first. For a completely 3D sand-grain covered bottom, such dependency of bottom roughness on flow

directions should not exist and $k_N \approx D$. Thus, the second scenario, which is the case for all tests in this study (e.g. photo of marble bottom shown in Fig. 2b), should have a k_N larger than D.

4. Characteristics of periodic turbulent oscillatory boundary layers

4.1. Vertical structures of periodic turbulent oscillatory boundary layers

The measured Reynolds-averaged velocity profiles are Fourier analyzed to reveal the vertical structures of periodic turbulent oscillatory boundary layers. Fig. 13 shows the amplitudes (U_1, U_2, U_3) and phases (φ_1, φ_2, φ_3) of the first three harmonics of a typical sinusoidal wave test SP400a_ce (the strongest sinusoidal wave over the ceramic-marble bottom). The gray zones indicate the variation in the longitudinal direction with their widths representing the standard deviations obtained from the spatial average. The standard deviations of U_1 and φ_1 are so small that they are not detectable when shown together with the spatial-averaged values, indicating very good longitudinal uniformity. Below a well-defined free-stream region (z>130mm), U_1 first increases a little to reach the maximum overshoot which is roughly 5% larger than the $U_{\infty,1}$ at about z=60mm, and then rapidly decreases towards the bottom. φ_1 starts to deviate from the free-stream value earlier than U_1, i.e. at roughly z=150mm. It slightly decreases until reaching a negative maximum overshoot ($-1°$) at about z=100mm, and then generally increases towards the bottom. At the lowest levels with valid measurements, z=5mm, φ_1 is about 22°. The second-harmonic velocity should theoretically not exist due to the symmetry of a sinusoidal variation. The measured U_2 is quite small (1.5∼3.5cm/s) and its vertical variation is quite unstruc-

tured, so it can be considered as experimental inaccuracy possibly related to sidewall and lid deflections. Compared to the second-harmonic velocity, the third-harmonic velocity is clearly meaningful. U_3 has a large overshoot below z=40mm which reaches 6.8cm/s. This cannot be associated with the merely 1$\sim$2cm/s magnitude of $U_{\infty,3}$. Its phase varies smoothly and rapidly by about 360° from z=80mm to z=5mm. Such a non-trivial third-harmonic velocity is also observed in other studies, e.g. Jonsson and Carlsen (1976). Trowbridge and Madsen (1984a) analytically showed that it is produced by the interaction of the time-varying turbulent eddy viscosity and the time-varying velocity.

Two typical tests in the fully rough turbulent regime, ST400a_ce and FL320a_ce, are chosen to represent the Stokes and forward-leaning waves, respectively. Fig. 14 shows the velocity amplitude and phase profiles of their first two harmonics. For easy comparison of the two tests, U_1 and U_2 are normalized by their free-stream amplitudes, and $\varphi_{\infty,2}$ is subtracted from the measured φ_2 to give the second-harmonic phase lead. The first-harmonic velocities of the two nonlinear waves have vertical structures very similar to that of the sinusoidal waves. The two φ_1 at z=5mm are almost the same (21° and 22°), which also agrees with test SP400a_ce. Thus, there is no significant effect of wave nonlinearities (represented by the second-harmonic velocity) on the vertical structures of the primary first harmonic. The measurements of second-harmonic velocities appear less smooth than the first-harmonic velocities possibly due to larger relative experimental error. U_2 generally follows the vertical variations of U_1. Judging from the locations of the overshoots, second harmonics have thinner boundary layers than the first harmonics. Al-

though the $\varphi_{\infty,2}$ of the two nonlinear waves differ by roughly 90°, the two profiles of the second-harmonic phase lead are very similar, except in the immediate vicinity of the bottom (z<10mm). The third-harmonic velocities show features similar to those of the sinusoidal waves, so they are not shown here.

4.2. Boundary layer thickness

A conventional definition of boundary layer thickness is the elevation where the velocity reaches 99% of the free-stream velocity. Inside turbulent oscillatory boundary layers both the velocity amplitudes and phases change with distance above bottom and the primary first harmonic has the thickest boundary layer. Therefore, a reasonable definition of the wave boundary layer thickness δ_w is where the velocity deficit of the complex first-harmonic velocity $U^{(1)} = U_1 e^{i\varphi_1}$ reaches 1%:

$$\frac{|U^{(1)}(\delta_w) - U_\infty^{(1)}|}{|U_\infty^{(1)}|} = 1\% \tag{18}$$

Among multiple locations satisfying Eq. (18), the highest one above the amplitude's maximum overshoot is taken as δ_w. To determine such a small 1% velocity deficit, the velocity measurements must be extremely accurate which was not achievable in most previous experimental studies. Thus, the elevation δ_m of the amplitude's maximum overshoot is often taken as an alternative measure of the boundary layer thickness, e.g. Jensen et al. (1989). Based on the standard deviation of spatial average, our relative error of measuring U_1 is generally less than 0.3%, and the error of measuring φ_1 is less than 0.1°. Thus, the relative measurement error for $U^{(1)}$ is:

$$|\frac{\epsilon(U^{(1)})}{U^{(1)}}| \approx |\frac{\epsilon(U_1)}{U_1} + i\epsilon(\varphi_1)| \approx 0.3\% \tag{19}$$

Since the spatial average is based on 20∼30 adjacent vertical velocity profiles, the relative 95%-confidence interval of $U^{(1)}$ is less than 0.1%. This is small enough for determining the 1% velocity deficit, so both δ_w and δ_m can be obtained experimentally in this study.

For turbulent oscillatory boundary layers over rough bottoms, the normalized boundary layer thicknesses, ζ_w=δ_w/k_N and ζ_m=δ_m/k_N, are single-valued functions of A_{bm}/k_N. For two nonlinear wave tests, since the dominant first harmonic is used to determine boundary layer thickness, $A_{bm,1}$=$U_{\infty,1}\omega^{-1}$ is taken as the representative A_{bm}. Fig. 15a shows the measurements of ζ_m from the present tests together with some measurements from other studies. For easy comparison, the measurements of smooth bottom tests are provided with k_N being the fitted effective bottom roughness k_b. Very good agreement between the present and previous studies is observed. The overall data set suggests that ζ_m increases with A_{bm}/k_N, in a manner approximated by a power law relationship ζ_m=$c_1(A_{bm}/k_N)^{c_2}$. Thus, a power-law fit is applied to the measurements (excluding smooth bottom tests) to get:

$$\zeta_m = \frac{\delta_m}{k_N} = 0.079 \cdot (\frac{A_{bm}}{k_N})^{0.81} \tag{20}$$

This is very close to the power-law relationship given by van der A et al. (2011) who obtained c_1=0.075 and c_2=0.82. The smooth bottom tests consistently have larger values of ζ_m than the prediction of the power-law fit by 40%±4%, which suggests that the smooth turbulent oscillatory boundary layers are systematically thicker.

Fig. 15b shows the measured ζ_w only from the present study, since no data from other studies are available for comparison. The rough-bottom measurements can be well represented by a straight line, which gives the

following power-law relationship:

$$\zeta_w = \frac{\delta_w}{k_N} = 0.192 \cdot (\frac{A_{bm}}{k_N})^{0.81} \tag{21}$$

An interesting finding is that ζ_w and ζ_m have identical values of c_2=0.81. Thus, the ratio ζ_w/ζ_m is nearly constant over the range $20<A_{bm}/k_N<1000$, and is equal to the ratio of c_1, i.e. 0.192/0.079=2.43. ζ_w of smooth bottom tests is again larger than the power-law prediction by about 63%±8%. Therefore, the systematic difference between the smooth and rough oscillatory turbulent boundary layers is even more significant for ζ_w. As will be discussed later, this is possibly due to the effect of secondary flows in the transverse plane.

4.3. Boundary layer streaming

Boundary layer streaming is obtained by averaging the Reynolds-averaged horizontal velocity over a wave period:

$$\bar{u}(z) = \int_0^T u(z,t)dt \tag{22}$$

For each bottom condition, the obtained boundary layer streaming profiles of three typical tests representing the three wave conditions are shown in Fig. 16. Since the two half-periods of a sinusoidal variation are completely symmetric, no boundary layer streaming should be expected. Thus, the measured $\bar{u}(z)$ of the three sinusoidal wave tests are only of the order mm/s and rather chaotically distributed around zero. However, for all nonlinear wave tests, the boundary layer streaming is clearly non-zero. The profiles have similar patterns of vertical variation, i.e. the streaming is negative in the near-bottom region, and then becomes positive at higher elevations. The

magnitude of this near-bottom negative streaming can be up to 1∼3cm/s and increases with bottom roughness. This is about 1∼3% of the maximum free-stream velocity, which is in agreement with other observations, e.g. van der A et al. (2011) for forward-leaning waves and Ribberink and Al-Salem (1995) for Stokes waves. According to Trowbridge and Madsen (1984b), this negative streaming is due to the interaction of the first-harmonic turbulent eddy viscosity and the first-harmonic Reynolds-averaged velocity. To balance the negative mean volume flux in the near-bottom region, a mean pressure gradient is developed to produce the observed positive streaming in the upper part of the boundary layer streaming profile.

4.4. Vertical velocity profiles

The Reynolds-averaged vertical velocities are Fourier analyzed to obtain the first three harmonics and the period-averaged velocity $\bar{w}$. The amplitudes of the first three harmonics are of the order mm/s and the phases have unorganized vertical variations, so the oscillatory vertical velocity is likely just the residual turbulence after the double average. However, meaningful period-averaged vertical velocities are observed. For the rough bottom tests shown in Fig. 17a and b, $\bar{w}$ is generally negative and can reach up to -9mm/s for the ceramic-marble bottom tests, but for smooth bottom tests shown in Fig. 17c, $\bar{w}$ is generally positive. Thus, $\bar{w}$ seems to be determined primarily by bottom conditions.

For steady turbulent flows in rectangular or square ducts, it has been shown that a Prandtl's secondary flow of the second kind characterized by streamwise vorticity is produced by the inhomogeneity of mean turbulence characteristics near boundaries of the cross section. For steady turbulent

flows in a smooth conduit with a square cross section, the flow near the corners is controlled by the bottom and the sidewall boundary layers, while the flow far away from the corners is only controlled by one boundary layer. Thus, in each quadrant of the square cross section, such a difference drives a pair of counter-rotating circulations which are symmetric around the corner's bisector and brings fluid toward the corner along the bisector (Hoagland, 1962), as shown in Fig. 18a. If the bottom is rough, the main inhomogeneity is the difference between the rough bottom boundary layer and smooth sidewall boundary layer, which produces an upward drift along the sidewalls and hence a downward drift along the vertical centerline (Fujita et al., 1989), as shown in Fig. 18b. The secondary flows have no dependency on the primary flow's direction, so the same circulation should be expected for oscillating flows in OWTs. Since the measurements shown in Fig. 17a, b and c are along the vertical centerline of the cross section and cover the 10cm near-bottom region (less than 1/4 of the channel's depth), $\bar{w}$ should be positive for the smooth bottom tests and negative for the rough bottom tests, which is corroborated by our observations. For the smooth bottom tests, as a confirmation, the $\bar{w}$ measured at one-quarter width from the sidewall is shown in Fig. 17d. The measurements are generally zero or slightly positive in the near-bottom part (z<40mm), and become negative at higher elevations, which agrees well with the secondary flow pattern along the black bar in Fig. 18a. For the rough bottom tests, since the ceramic-marble bottom tests have higher turbulence intensity in the bottom boundary layer than the "sandpaper" bottom tests, their secondary flows should be relatively stronger, which is confirmed by our measurements. Therefore, the observed $\bar{w}$ clearly indicates the existence of

a secondary flow in the transverse plane of the test channel.

Since $\bar{w}$ is mostly downward for rough bottom tests, it will transfer the high momentum of the free-stream region into the bottom boundary layer, so the boundary layer is consolidated. However, for smooth bottom tests, the upward $\bar{w}$ will transfer the low momentum fluid within the bottom boundary layer into the free-stream region, and the boundary layer is stretched. This can possibly explain why the smooth bottom boundary layers seem to be "thicker" than the rough bottom boundary layers, especially for ζ_w, as shown in Fig. 15. Meanwhile, this also implies that the observed rough bottom boundary layers may be thinner than those of real coastal waves, so the fitted power-law formulas may just work for periodic waves in OWTs.

5. Bottom shear stress

5.1. Log-profile fitting method

The momentum equation for oscillatory turbulent boundary layers in OWTs is:

$$\frac{\partial u}{\partial t} = -\frac{\partial p/\rho}{\partial x} + \frac{\partial(\tau/\rho)}{\partial z} \tag{23}$$

where τ/ρ is simply called shear stress hereafter. Since the $\partial u/\partial t$ term is negligibly small compared to other terms in the very near-bottom region, the flow can be considered quasi-steady, i.e. at any instance, t, the near-bottom flow should follow a logarithmic distribution controlled by $\tau_b(t)/\rho$ and k_b. Therefore, we can perform log-profile fitting to obtain $u_*(t)$. The instantaneous bottom shear stress is then given by:

$$\frac{\tau_b(t)}{\rho} = |u_*(t)|u_*(t) \tag{24}$$

Fig. 19 shows the double-averaged instantaneous velocity profiles and the fitted logarithmic profiles for test SP400a_ce. For clarity, only the region z<50mm is shown for half of the wave period. To have sufficient but not too many data points, the log-profile fittings are simply based on the bottom-most five data points which satisfy the data selection rules for fitting the first-harmonic amplitude profile. For most instantaneous velocity profiles, the fitted logarithmic profiles reasonably pass through the selected data points, and the fitted k_b has a mean value of 19.3mm with a 6.3mm standard deviation, which agrees well with the k_b=k_N=20mm obtained before. However, the three velocity profiles, identified by bright red symbols, in the time window from ωt=68° to 90° give instantaneous k_b that differ from k_b=20mm by a factor over 4. This time window corresponds to when the free-stream velocity $u_\infty(t)$ crosses zero. As $u_\infty(t)$ decreases to zero, $\partial p/\partial x$ has the same sign of $u_\infty(t)$ and generally increases with ωt. Therefore, the oscillatory flow experiences an increasingly adverse pressure gradient, which eventually leads to separation of boundary layers (near-bottom velocities opposing the free-stream velocity), e.g. at ωt=79°. In such situations, the near-bottom logarithmic layer vanishes. The total duration when the log-profile fitting is not applicable is roughly about 20∼30% of T for all periodic wave tests in this study. Thus, the log-profile fitting method still works during most of a wave period.

Since k_b is already obtained from fitting the first-harmonic amplitude profile, $u_*(t)$ can be determined through a modified log-profile fitting which has a predetermined z_0=k_b/30. This will significantly smooth the obtained time series of $u_*(t)$, as shown in Fig. 20. At the instants when the very

near-bottom logarithmic profile disappears, $u_*(t)$ is close to zero, so it is still acceptable to apply the modified log-profile fittings to the bottom-most five points and use the fitted $u_*(t)$, which is also close to zero, as a rough estimate of the actual $u_*(t)$.

5.2. Momentum integral method

The shear stress at any vertical elevation z can be estimated by integration of Eq. (23):

$$\frac{\tau(z,t)}{\rho} = \int_z^{z_\delta} \frac{\partial[u_\infty(t) - u(z',t)]}{\partial t} dz' \tag{25}$$

where the free-stream level z_δ should be outside the boundary layer. For all tests, z_δ is between 1.3 and 1.5 times the boundary layer thickness δ_w obtained in Section 4.2, ensuring that $\tau(z_\delta,t)/\rho$ is zero. Eq. (25) can be expressed in terms of Fourier components:

$$\frac{\tau(z)^{(n)}}{\rho} = \int_z^{z_\delta} in\omega(U_\infty^{(n)} - U(z')^{(n)})dz' \tag{26}$$

Thus, the n-th-harmonic shear stress $\tau(z)^{(n)}/\rho$ can be obtained by integrating the n-th-harmonic velocity deficit. The bottom shear stress is often evaluated at z=z_0 which is below the lowest level with valid measurements z=z_1. Thus, the integral for bottom shear stress is:

$$\frac{\tau_b^{(n)}}{\rho} = \int_{z_1}^{z_\delta} in\omega(U_\infty^{(n)} - U^{(n)})dz + \int_{z_0}^{z_1} in\omega(U_\infty^{(n)} - U^{(n)})dz \tag{27}$$

The second part is essentially an extrapolation of the first part, and it must be calculated using extrapolated distributions of amplitude U_n and phase φ_n of nth-harmonic velocity from z_0 to z_1. For the first-harmonic velocity, the amplitude U_1 is extrapolated by extending the logarithmic profile given by the

log-profile fitting. For the phase of the first-harmonic velocity φ_1, we simply propose a depth-invariant extrapolation of the measured φ_1 at $z{=}z_1$. Since other logical extrapolations, e.g. linear or quadratic extrapolation, makes virtually no difference. Table 7 shows the amplitudes and phases of the first-harmonic bottom shear stress given by the momentum integral method for three representative tests over the ceramic-marble bottom. The amplitude of the extrapolation term (the third column) can be up to 50% of the numerical-integral term based on actual measurements (the second column), and they do not have similar phases, i.e. roughly 76° versus 1∼10°. Both the "sandpaper" bottom and the smooth bottom yield the same comparison. For any experimental methodology which contains such a large extrapolated component, the obtained results are inherently questionable, unless the extrapolation has very solid physics background. For smooth bottom tests, our proposed extrapolation of velocity, although not perfect, is still an acceptable representation of the actual velocity distribution. However, for rough bottom tests, part of the extrapolation layer, called the roughness layer hereafter, is occupied by solid roughness elements, which makes the concept of a "fluid velocity" completely fictitious. Thus, any assumed distribution of velocity, including ours, is questionable. For the same reasons, we will not discuss the extrapolation for higher order harmonics.

5.3. Reynolds stress method

All tests in this study are highly turbulent, so the Reynolds stress calculated using Eq. (5) is the dominant mechanism for transfer of momentum across boundary layers, and can be considered the shear stress which controls the Reynolds-averaged flow. Ideally, the obtained vertical profiles of

Reynolds stress should be identical to those given by the momentum integral method. Fig. 21 shows the comparisons based on the first-harmonic shear stress of a typical sinusoidal wave, SP400a, over our three bottom configurations. Clearly, the Reynolds stresses are generally smaller than the shear stresses given by the momentum integral method. At about z=5mm, for tests over the smooth and the "sandpaper" bottoms the Reynolds stresses are roughly 50% of those obtained from the momentum integral method, but for the test over the ceramic-marble bottom this ratio increases to about 75%, so the discrepancy seems to decrease with bottom roughness. Moreover, the discrepancy also decreases with elevation and the elevation z_{match} where the two methods become identical decreases with bottom roughness, i.e. z_{match} is 80mm for the smooth bottom test, but decreases to 38mm and 18mm for the "sandpaper" and ceramic-marble bottoms, respectively.

These discrepancies are due to the PIV's limited ability to measure turbulent fluctuations. As introduced in Section 2.2, the PIV cross-correlation analysis is based on interrogation grids with length and depth scales of O(1mm). This algorithm essentially serves as a low-pass filter which removes all turbulent eddies smaller than the size of the interrogation grids, so the contribution from these small eddies to the total Reynolds stress is missed. According to the mixing length theory, the characteristic scale of eddies increases with elevation, so less eddies are missed in the upper part of the boundary layer, which leads to better agreement between the two methods. Since the characteristic scale of the turbulent eddies in close vicinity to the bottom is proportional to the physical scale of bottom roughness elements and the three tests shown in Fig. 21 have identical sizes of the interrogation

grids, smoother bottom leads to smaller turbulent eddies and consequently more severe underestimate of Reynolds stress. To further prove our arguments, the Reynolds stresses of test SP400a_sa given by two PIV resolutions are shown in Fig. 22. The coarse resolution is about twice the fine resolution, and affords a roughly 20% smaller Reynolds stress below z=40$\sim$50mm. The phase profiles, Fig. 21b, d and f, show good agreement between the two methods, except for the region close to the upper edge of the boundary layer where the momentum integral is subject to experimental error, since $U^{(1)}$-$U_\infty^{(1)}$ becomes vanishingly small. If we consider the total Reynolds stress as the sum of contributions from missed and captured eddies, this good agreement in phase indicates that the two contributions are generally in phase, so missing some small eddies only reduces the amplitude. This hypothesis is further supported by the excellent agreement between the two phase profiles shown in Fig. 22b. Most velocity measurement instruments, such as PIV, require a finite sampling volume with scales of O(mm) to provide measurements, so they are all subject to the effect of "missing" eddies. This is the likely reason why almost all existing experimental studies have reported that the measured Reynolds stress was smaller than that obtained from the momentum integral method, e.g. van der A et al. (2011) and Hay et al. (2012b).

5.4. Momentum integral versus log-profile fitting

The comparison between the momentum integral method and the log-profile fitting method is based on their determination of the first-harmonic amplitude and phase of the bottom shear stress. The comparison for the three bottom configurations are shown in Table 8. For tests over the smooth bottom, the two methods give nearly identical estimates of the first-harmonic

bottom shear stress, i.e. the average ratio of amplitudes is 100%±14% and the average offset in phases is $-3.2°\pm4.6°$. This good agreement suggests that both methods are valid for estimating bottom shear stress for smooth oscillatory turbulent boundary layer flows. As an additional piece of evidence, Jensen et al. (1989) in their smooth bottom tests directly measured the bottom shear stress using hot-film probes and found that the direct measurements were in good agreement with the bottom shear stresses given by log-profile fittings. However, this good agreement disappears when the bottom becomes rough, with the first-harmonic bottom shear stress afforded by the momentum integral method becoming systematically smaller than that of the log-profile fitting method as the bottom roughness increases. The average ratio of amplitudes drops to 72%±9% for tests over the "sandpaper" bottom, and is further reduced to 58%±6% for tests over the ceramic-marble bottom. Since the log-profile fitting method is based on a quasi-steady assumption which is independent of whether the bottom is smooth or rough, it is legitimate to extend its confirmed validity for smooth bottom scenarios to rough bottom scenarios. Therefore, the observed discrepancy suggests that the momentum integral method is questionable.

As shown in Section 4.4, we observed a mean vertical velocity due to secondary flows in the transverse plane, which leads to an additional term in the governing equation:

$$\frac{\partial u}{\partial t} = \frac{\partial u_\infty}{\partial t} + \frac{\partial \tau/\rho}{\partial z} - \bar{w}\frac{\partial u}{\partial z} \tag{28}$$

The first harmonic of this equation can be integrated from z to z_δ to yield:

$$MI(z)^{(1)} = \tau(z)^{(1)}/\rho - \int_z^{z_\delta} \bar{w}\frac{\partial(U_\infty^{(1)} - U(z)^{(1)})}{\partial z'}dz' \tag{29}$$

where $MI(z)^{(1)}$ is the complex first harmonic of the momentum integral. In this form it is readily recognized that the momentum integral is the actual shear stress $\tau(z)$ minus the influence of the non-zero mean vertical velocity component which represents the "error" of the momentum integral method. We simply integrate this error term by parts to obtain:

$$\begin{aligned} -\int_z^{z_\delta} \bar{w}\frac{\partial(U_\infty^{(1)} - U^{(1)})}{\partial z'}dz' = \\ \bar{w}(U_\infty^{(1)} - U^{(1)}) + \int_z^{z_\delta} \frac{\partial \bar{w}}{\partial z}(U_\infty^{(1)} - U^{(1)})dz' \end{aligned} \tag{30}$$

The second term on the right-hand side is scaled by the vertical gradient of the mean vertical velocity. A rough estimate based on Fig. 17 suggests that it is less than $0.1s^{-1}$, which is considered much smaller than the angular frequency ω=0.5 or $1s^{-1}$ in this study. Thus, this term is negligibly small compared to $MI(z)^{(1)}$, and consequently only the first term could result in a sizeable error. In the near-bottom region, the phases of $U^{(1)}$ in Eq. (29), of the order 20°, has little influence on their amplitudes, which gives:

$$|MI^{(1)}| \approx |\tau^{(1)}/\rho| + \bar{w}(z)(|U_\infty^{(1)}| - |U^{(1)}|) \tag{31}$$

Apparently, the momentum integral will underestimate or overestimate the shear stress if $\bar{w}$ is negative or positive. As the velocity deficits increase towards the bottom, the error term also grows and the momentum integral becomes increasingly incorrect. At z=z_0, we have:

$$|I_b^{(1)}| = |\tau_b^{(1)}/\rho| + \bar{w}_b|U_\infty^{(1)}| \tag{32}$$

For rough bottom tests, z=z_0 is a fictitious bottom level which does not necessarily require a zero $\bar{w}$, e.g. for the ceramic-marble bottom there is

still 9mm space from z=z_0 to the solid surface of aluminum plates. Thus, a non-zero $\bar{w}$ can exist inside the roughness layer. As shown in Fig. 17b, $\bar{w}$ even increases towards the bottom below z=20mm, which is also observed for the gravel-bottom tests of van der A et al. (2011). The error term is essentially a net downward transfer of momentum which drives (together with the pressure gradient) the flow around individual roughness elements as well as the "porous flow" below z=z_0 to produce a form drag. The momentum integral method fails to capture this, and consequently underestimates the bottom shear stress. If we use the bottom-most $\bar{w}$ for $\bar{w}_b$, the obtained error terms are $-24cm^2/s^2$ and $-96cm^2/s^2$ for tests SP400a_sa and SP400a_ce, respectively, which correspond to 16% and 30% of the $\tau_b^{(1)}$ given by the log-profile fitting method. These are comparable to the observed discrepancies, i.e. 28% and 42%. For smooth bottom tests, even though the observed $\bar{w}$ may not approach zero towards the bottom due to some unknown experimental error, there is no question that $\bar{w}_b$ must be zero at z=0≈z_0. Thus, the error term vanishes and the momentum integral is still able to give the correct bottom shear stress for smooth bottom tests.

In conclusion, among the methods to infer bottom shear stress from velocity measurements, only the log-profile fitting method can be considered to yield the correct estimate.

5.5. Friction factors and phase leads

The maximum bottom shear stress τ_{bm}/ρ and its phase lead relative to the maximum free-stream velocity $\varphi_{\tau bm}$ are very important parameters for practical applications. Here we only consider the τ_{bm}/ρ and $\varphi_{\tau bm}$ for sinusoidal wave tests, because the nonlinear wave tests in OWTs may have a sizeable

mean bottom shear stress due to the facility-produced return current which affects τ_{bm}/ρ, as discussed by Yuan (2013). It is customary to express τ_{bm}/ρ in terms of a wave friction factor f_w introduced by Jonsson (1966):

$$f_w = 2\frac{\tau_{bm}/\rho}{U_{\infty,1}^2} \tag{33}$$

For sinusoidal oscillatory turbulent boundary layers, the bottom shear stress should only contain odd Fourier components for which the amplitudes decay quickly with orders. Therefore, to remove experimental noise, τ_{bm} is determined from a smoothed $\tau_b(t)$ by only retaining its first and third harmonics, i.e. the thick solid line in Fig. 23.

In Fig. 24, the results of f_w and $\varphi_{\tau bm}$ are compared with some previous experimental studies which have reliable measurements of bottom shear stress. For the smooth bottom tests of Jensen et al. (1989), the effective bottom roughness k_b is evaluated using the formula, k_b=$1.32 \cdot 3.3\nu/u_{*m}$, as discussed in Section 3.2.1. The measurements of f_w have very good consistency, while the measurements of $\varphi_{\tau bm}$ show relatively larger scatter. This is probably because the phase is more sensitive to experimental noise. Nevertheless, it is clear that both parameters decrease with increasing A_{bm}/k_b. For smooth bottom tests, our measurements of f_w agree excellently with the measurements of Jensen et al. (1989), but the values of $\varphi_{\tau bm}$ from the present study are higher by roughly 5°. The reason for this is unclear, but the discrepancy is not vital. Recently, Humbyrd (2012) proposed an improved version of the Grant and Madsen (1979) model without empirically determined parameters. For $10<A_{bm}/k_b<10^5$, her model gives:

$$f_w = \exp(5.70(\frac{A_{bm}}{k_b})^{-0.101} - 7.46) \tag{34}$$

$$\varphi_{\tau bm}[rad] = 0.649(\frac{A_{bm}}{k_b})^{-0.160} + 0.118 \tag{35}$$

As shown in Fig. 24, the measured f_w tightly follow the prediction, and the measured $\varphi_{\tau bm}$ are evenly distributed around the predicted curve, except for the three points given by Jensen et al. (1989). Therefore, the model can predict the maximum bottom shear stress with excellent accuracy.

To reveal the intra-period variation of bottom shear stress for linear (sinusoidal) or nonlinear (Stokes and forward-leaning) waves, $\tau_b(t)/\rho$ is fourier analyzed to give the first three harmonics of bottom shear stress. The mean bottom shear stress is not shown here, because it will be intensively discussed in a forthcoming journal publication focusing on experimental results obtained in our OWT for combined wave-current boundary layer flows. Gonzalez-Rodriguez and Madsen (2011) developed an analytical model based on a time-varying turbulent eddy viscosity. For a free-stream velocity given by the sum of the first and second harmonics, e.g. Eq. (6), they analytically obtained the first three harmonics of bottom shear stress which are expressed in terms of friction factors and phase leads:

$$\frac{2\tau_b^{(1)}/\rho}{U_{\infty,1}^2} = f_1 \exp(i\varphi_{\tau b,1}) \tag{36}$$

$$\frac{2\tau_b^{(2)}/\rho}{U_{\infty,1}U_{\infty,2}} = f_2 \exp[i(\varphi_{\tau b,2} + \varphi_{\infty,2})] \tag{37}$$

$$\frac{2\tau_b^{(3)}/\rho}{U_{\infty,1}^2} = f_3 \exp(i\varphi_{\tau b,3}) \tag{38}$$

The model prediction suggests that the effect of the $U_\infty^{(2)}$ on the first and third harmonics of bottom shear stress is negligible for realistic values of $U_\infty^{(2)}$ ($<U_\infty^{(1)}/4$). Therefore, (f_1, f_3) and ($\varphi_{\tau b,1}$, $\varphi_{\tau b,3}$) can be considered single-valued functions of $A_{bm,1}/k_b$, while f_2 and $\varphi_{\tau b,2}$ are functions of $A_{bm,1}/k_b$ and

$\varphi_{\infty,2}$. These dependencies are further approximated by the explicit formulas (not shown here for simplicity) given by Gonzalez-Rodriguez and Madsen (2010) (hereafter GRM10). For easy comparison, our measurements are also expressed in term of these friction factors and phase leads.

The first-harmonic bottom shear stress, $\tau_b^{(1)}$, is the dominant component of bottom shear stress. The measurements of f_1, Fig. 25a, exhibit little scatter and nicely form a decreasing trend. No visually detectable difference among the three wave conditions is observed. Similar to $\varphi_{\tau bm}$, the measured $\varphi_{\tau b,1}$, Fig. 25b, decreases as $A_{bm,1}/k_b$ increases. The $\varphi_{\tau b,1}$ of the forward-leaning waves appears slightly smaller than those of the other two wave conditions. This is possibly because $\varphi_{\tau b,1}$ is relatively more sensitive to the effect of $U_\infty^{(2)}$ than f_1. Nevertheless, the difference (less than 5°) is small enough to be considered negligible. The second-harmonic bottom shear stress ,$\tau_b^{(2)}$, is present only for nonlinear waves and partly depends on $\varphi_{\infty,2}$, so we obtain two curves in Fig. 25c and d. The measurements suggest that the f_2 of Stokes waves is slightly smaller than those of forward-leaning waves. For $\varphi_{\tau b,2}$, the data points show a systematic difference between the two wave conditions, i.e. the $\varphi_{\tau b,2}$ of forward-leaning waves are larger than those of Stokes waves by roughly 5∼10°. The third-harmonic bottom shear stress $\tau_b^{(3)}$ is much smaller than $\tau_b^{(1)}$ and $\tau_b^{(2)}$ in amplitude, so larger scatter is observed for both f_3 and $\varphi_{\tau b,3}$, as shown in Fig. 25e and f. Nevertheless, the measurements suggest that both f_3 and $\varphi_{\tau b,3}$ decrease with increasing $A_{bm,1}/k_b$. It should be noted that the ratio f_3/f_1 is in general between 10∼16%. Thus, although $U^{(3)}$ is very small, $\tau_b^{(3)}$ is a non-negligible part of the total bottom shear stress. This is because $\tau_b^{(3)}$ is mainly produced by the interaction of the

second-harmonic turbulent eddy viscosity and the first-harmonic velocity, as suggested by Trowbridge and Madsen (1984a).

The measured friction factors and phase leads are reasonably predicted by the GRM10 model. For $\tau_b^{(1)}$, the model sightly underestimates f_1 and overestimates $\varphi_{\tau b,1}$ in the low $A_{bm,1}/k_b$ regime, but the model's performance improves with increasing $A_{bm,1}/k_b$. Given the smallness of $\tau_b^{(3)}$ and the large scatter, the predictions of f_3 and $\varphi_{\tau b,3}$ are sufficiently good. For $\tau_b^{(2)}$, the GRM10 model reasonably predicts $\varphi_{\tau b,2}$ for each wave condition, and captures the observed difference between Stokes and forward-leaning waves quite well. However, it underestimates f_2 by up to 20∼30% for low values of $A_{bm,1}/k_b$. This may be a significant problem, because the second-harmonic bottom shear stress plays a major role in producing a net sediment transport in the wave direction. Therefore, it would be desirable to improve the predictive skills of the model developed by Gonzalez-Rodriguez and Madsen (2011) for the second-harmonic shear stress characteristics.

6. Conclusion

A high-quality experimental study including a large number of tests which correspond to full-scale coastal boundary layer flows is performed using a state-of-the-art oscillating water tunnel for flow generations and a Particle Image Velocimetry system for velocity measurements. The tests include three wave shapes: Sinusoidal, Stokes and Forward-leaning waves, over three different bottom roughness configurations: smooth, "sandpaper" and ceramic-marble bottoms.

Experimental results show that the logarithmic profile can accurately

represent the near-bottom first-harmonic amplitude of sinusoidal oscillatory flows, and the log-profile fitting give highly accurate determinations of bottom roughness and theoretical bottom location z=0. For smooth bottom tests, it is demonstrated that the effective bottom roughness formula for steady smooth turbulent flows suggested by Nikuradse (1932), $k_b = 3.3\nu/u_*$, is also applicable for smooth turbulent oscillatory flows if the characteristic shear velocity is based on a period-averaged value. The definition of this shear velocity requires future experimental investigations. For the "sandpaper" bottom, tests over a wide range of Re_*, (from 33 to 611) show that k_b varies with Re_* in a pattern similar to but not in quantitative agreement with Nikuradse (1933). Thus, the curve $C(Re_*)$ from Nikuradse's study, which is often used to determine k_b, is not universally applicable. For the ceramic-marble bottom, all tests are in the fully rough turbulent regime. The obtained z=0 is $0.32D$ below the crests of the uniform ceramic marbles, and the fitted k_b=k_N is consistently larger than D, i.e. k_N=$1.6D$. This is because of flow alignment relative to the regular pattern of marble placement.

The Reynolds-averaged horizontal velocity is Fourier analyzed to reveal the detailed vertical structures of turbulent oscillatory boundary layers. The first harmonics of both sinusoidal and nonlinear waves, as well as the second harmonic of nonlinear waves, exhibit similar patterns of vertical variation, i.e. the amplitudes have a small overshoot and the phases generally increase toward the bottom. For nonlinear waves, a weak boundary layer streaming is observed. It is in the negative direction (against the wave direction) in the very near-bottom region, and becomes positive further away from the bottom due to a superimposed mean pressure gradient. This, as well as a small

but meaningful third harmonic embedded in both sinusoidal and nonlinear waves can be only explained by the interaction of a time-varying turbulent eddy viscosity and the time-varying near-bottom velocity, as suggested by Trowbridge and Madsen (1984a,b). Two dimensionless characteristic boundary layer thicknesses, the elevation ζ_w of 1% complex first-harmonic velocity deficit and the elevation of the maximum first-harmonic amplitude overshoot ζ_m, are measured. For rough bottom tests, both of them have power-law dependencies on the relative roughness A_{bm}/k_N. The ratio ζ_w/ζ_m is consistently about 2.4 over the range $20<A_{bm}/k_N<1000$. The smooth oscillatory turbulent boundary layers are found to be 40$\sim$65% thicker than the predictions given by the power-law fits based on rough turbulent wave boundary layers. Observations show that the period-averaged vertical velocity measured in the 10cm near-bottom region along the vertical centerline of the cross section is generally positive for smooth bottom tests, but generally negative for the rough bottom tests, due to different patterns of Prandtl's secondary flows of the second kind.

Three methods, log-profile fitting, momentum integral and Reynolds stress, to infer the bottom shear stress from velocity measurements are discussed. The comparison between the momentum integral method and the Reynolds stress method suggests that the Reynolds stress method yields smaller estimates of the bottom shear stress than the momentum integral method. This is because turbulent eddies with physical scales smaller than the PIV's interrogation grids are not captured in the PIV cross-correlation analysis, and consequently their contributions to the Reynolds stress are missed. The comparison between the momentum integral method and the log-profile fitting

method suggests that the momentum integral method gives a significantly smaller estimate of bottom shear stress for rough bottom tests. This is due to the non-zero mean vertical velocity associated with the secondary flow in the transverse plane, which produces a net transfer of momentum at the conceptual bottom level where the bottom shear stress is estimated. In addition, the momentum integral method requires a sizeable extrapolation based on a fictitious velocity distribution within the roughness layer, which makes the method inherently questionable. Therefore, among the three possible methods, only the log-profile fitting method is considered to yield the correct estimate of the bottom shear stress.

For sinusoidal wave boundary layers, the measurements suggest that both the maximum bottom shear stress (in terms of the wave friction factor) and the associated phase lead decrease with the relative roughness. These variations are accurately predicted by the Humbyrd (2012) model which represents the latest version of Grant-Madsen-type models. A sizeable third-harmonic bottom shear stress which is up to 15% of the dominant first-harmonic bottom shear stress is observed. Both of these two significant harmonics are well predicted by the GRM10 model which assumes a time-varying turbulent eddy viscosity. For nonlinear waves, the measurements suggest that first and third-harmonic bottom shear stresses receive little influence from the wave nonlinearities. A sizeable second-harmonic bottom shear stress which weakly depends on the wave shape is observed. The analytical model developed by Gonzalez-Rodriguez and Madsen (2011) which is represented by approximate explicit formulas given by Gonzalez-Rodriguez and Madsen (2010) reasonably predicts its phase but underestimates its amplitude by up to 20% for

low values of $A_{bm,1}/k_b$, implying that this model would benefit from further improvements.

Acknowledgements

We gratefully acknowledge the financial support for this research from the National Research Foundation of Singapore (NRF) through the Singapore-MIT Alliance for Research and Technology's (SMART) Center for Environmental Sensing and Modeling (CENSAM) program.

References

van der A, D.A., O'Donoghue, T., Davies, A.G., Ribberink, J.S., 2011. Experimental study of the turbulent boundary layer in acceleration-skewed oscillatory flow. Journal of Fluid Mechanics 684, 251–283.

Abreu, T., Michallet, H., Silva, P.A., Sancho, F., van der A, D.A., Ruessink, B.G., 2013. Bed shear stress under skewed and asymmetric oscillatory flows. Coastal Engineering 73, 1–10.

Bayazit, M., 1976. Free surface flow in a channel of large relative roughness. Journal of Hydraulic Research 14, 115–126.

Brevik, I., 1981. Oscillatory rough turbulent boundary layers. Journal of the Waterway Port Coastal and Ocean Division 107, 175–188.

Cox, D.T., Kobayashi, N., Okayasu, A., 1996. Bottom shear stress in the surf zone. Journal of Geophysical Research: Oceans 101(C6), 14337–14348.

Davies, A.G., Soulsby, R.L., King, H.L., 1988. A numerical model of the combined wave and current bottom boundary layer. Journal of Geophysical Research: Oceans 93(C1), 491–508.

Dixen, M., Hatipoglu, F., Sumer, B.M., Fredsøe, J., 2008. Wave boundary layer over a stone-covered bed. Coastal Engineering 55, 1–20.

Fredsøe, J., 1984. Turbulent boundary layer in wave-current motion. Journal of Hydraulic Engineering 110, 1103–1120.

Fujita, H., Yokosawa, H., Hirota, M., 1989. Secondary flow of the second kind in rectangular ducts with one rough wall. Experimental Thermal and Fluid Science 2, 72–80.

Gonzalez-Rodriguez, D., Madsen, O.S., 2010. Prediction of net bedload transport rates obtained in oscillating water tunnels and applicability to real surf zone waves. Proc. 32nd International Conference on Coastal Engineering , sediment–21.

Gonzalez-Rodriguez, D., Madsen, O.S., 2011. Boundary-layer hydrodynamics and bedload sediment transport in oscillating water tunnels. Journal of Fluid Mechanics 667, 48–84.

Grant, W.D., 1977. Bottom friction under waves in the presence of a weak current: its relationship to coastal sediment transport. Ph.D. thesis. Massachusetts Institute of Technology. Cambridge, MA, U.S.

Grant, W.D., Madsen, O.S., 1979. Combined wave and current interaction with a rough bottom. Journal of Geophysical Research: Oceans 84(C4), 1797–1808.

Hay, A.E., Zedel, L., Cheel, R., Dillon, J., 2012a. Observations of the vertical structure of turbulent oscillatory boundary layers above fixed roughness beds using a prototype wideband coherent doppler profiler: 1. the oscillatory component of the flow. Journal of Geophysical Research: Oceans 117, C03005.

Hay, A.E., Zedel, L., Cheel, R., Dillon, J., 2012b. Observations of the vertical structure of turbulent oscillatory boundary layers above fixed roughness using a prototype wideband coherent doppler profiler: 2. turbulence and stress. Journal of Geophysical Research: Oceans 117, C03006.

Hoagland, L., 1962. Fully developed turbulent flow in straight rectangular ducts-secondary flow, its cause and effect on the primary flow. Ph.D. thesis. Massachusetts Institute of Technology. Cambridge, MA, U.S.

Holmedal, L.E., Myrhaug, D., 2006. Boundary layer flow and net sediment transport beneath asymmetrical waves. Continental Shelf Research 26, 252–268.

Humbyrd, C.J., 2012. Turbulent combined wave-current boundary layer model for application in coastal waters. Master's thesis. Massachusetts Institute of Technology. Cambridge, MA, U.S.

Jensen, B.L., Sumer, B.M., Fredsøe, J., 1989. Turbulent oscillatory boundary layers at high reynolds numbers. Journal of Fluid Mechanics 206, 265–297.

Jiménez, J., 2004. Turbulent flows over rough walls. Annual Review of Fluid Mechanics 36, 173–196.

Jonsson, I.G., 1963. Measurements in the turbulent wave boundary layer. Proc 10th Congr, IAHR, London 1, 85–92.

Jonsson, I.G., 1966. Wave boundary layer and friction factors, in: Proceedings of the 10th International Conference on Coastal Engineering, ASCE. pp. 127–148.

Jonsson, I.G., Carlsen, N.A., 1976. Experimental and theoretical investigations in an oscillatory turbulent boundary layer. Journal of Hydraulic Research 14, 45–60.

Kajiura, K., 1968. A model of bottom boundary layer in water waves. Bull. Earthquake Res. lnst., Univ. Tokyo 46, 75–123.

Kemp, P.H., Simons, R.R., 1982. The interaction between waves and a turbulent current: waves propagating with the current. Journal of Fluid Mechanics 116, 227–250.

Kemp, P.H., Simons, R.R., 1983. The interaction of waves and a turbulent current: waves propagating against the current. Journal of Fluid Mechanics 130, 73–89.

Krstic, R.V., Fernando, H.J.S., 2001. The nature of rough-wall oscillatory boundary layers. Journal of Hydraulic Research 39, 655–666.

Lavelle, J., Mofjeld, H., 1983. Effects of time-varying viscosity on oscillatory turbulent channel flow. Journal of Geophysical Research: Oceans 88(C12), 7607–7616.

Longuet-Higgins, M.S., 1953. Mass transport in water waves. Philosophical Transactions of the Royal Society of London. Series A, Mathematical and Physical Sciences 245, 535–581.

Lundgren, H., Sorensen, T., 1957. A pulsating water tunnel, in: Proc. 6th International Conference on Coastal Engineering, pp. 356–358.

Nikuradse, J., 1932. Gesetzmässigkeiten der turbulenten strömung in glatten rohren. Ver. Dtsch. Ing. Forsch. 3, 1–36.

Nikuradse, J., 1933. Strömungsgesetze in rauhen rohren. Ver. Dtsch. Ing. Forsch. 361.

Ribberink, J.S., Al-Salem, A.A., 1995. Sheet flow and suspension of sand in oscillatory boundary layers. Coastal Engineering 25, 205–225.

Scandura, P., 2007. Steady streaming in a turbulent oscillating boundary layer. Journal of Fluid Mechanics 571, 265–280.

Sleath, J.F.A., 1987. Turbulent oscillatory flow over rough beds. Journal of Fluid Mechanics 182, 369–409.

Sleath, J.F.A., 1991. Velocities and shear stresses in wave-current flows. Journal of Geophysical Research: Oceans 96(C8), 15237–15244.

Trowbridge, J., Madsen, O.S., 1984a. Turbulent wave boundary layers: 1. model formulation and first-order solution. Journal of Geophysical Research: Oceans 89(C5), 7989–7997.

Trowbridge, J., Madsen, O.S., 1984b. Turbulent wave boundary layers: 2. second-order theory and mass transport. Journal of Geophysical Research: Oceans 89(C5), 7999–8007.

van der Werf, J.J., Schretlen, J.J.L.M., Ribberink, J.S., O'Donoghue, T., 2009. Database of full-scale laboratory experiments on wave-driven sand transport processes. Coastal Engineering 56, 726–732.

Yuan, J., 2013. Experimental and theoretical study of turbulent oscillatory boundary layers. Ph.D. thesis. Massachusetts Institute of Technology. Cambridge, MA, U.S.

Yuan, J., Madsen, O., Chan, E.S., 2012. Experimental study of turbulent oscillatory boundary layers in a new oscillatory water tunnel. Proc. 33rd International Conference on Coastal Engineering , waves–24.

Figure captions

Figure 1. 3D Sketch of the Wave-Current-Sediment (WCS) facility.

Figure 2. Rough Bottom: (a) "sandpaper" bottom (top-view), (b) ceramic-marble bottom (top-view), (c) "sandpaper" bottom (side-view), (d) ceramic-marble bottom (side-view).

Figure 3: Free-steam velocities of nonlinear oscillatory flows (solid line: Stokes wave, dashed line: forward-leaning wave).

Figure 4: A small part of the PIV image showing the bottoms (yellow dashed lines: y=0 of the temporary vertical coordinate y): (a) smooth bottom, (b) ceramic-marble bottom, (c) "sandpaper" bottom (black curve: the bottom profile given by normal-distribution fittings).

Figure 5: Normal-distribution fitting of the 50-pixel-averaged smooth bottom brightness profile (solid line: fitted curve, crosses: selected data points, dots: measured brightness profile).

Figure 6: Bottom profile of the smooth bottom determined from normal-distribution fitting: (a) the obtained bottom profile (dots) with the 95%-confidence interval (error bars) and a linear fit (solid line), (b) the temporal variation of the bottom location Z_0 at X=1025 during wave generation, SP400a (full circles: measurements, solid line: a fitted sinusoidal variation).

Figure 7: The coefficient of determination for log-profile fitting 1-R^2 as a function of zero offset Δ: (a) ceramic-marble bottom, (b) "sandpaper" bottom.

Figure 8: Dimensionless measured velocity profiles and fitted logarithmic profiles over the smooth bottom (data points between the two "×" markers are used for log-profile fittings): (a) pure current test C40_sm, (b) sinusoidal

wave test SP400a_sm.

Figure 9: Dependency of C on Re_* for the "sandpaper" bottom (error bars indicate 95%-confidence interval).

Figure 10: Measured velocity profiles and fitted logarithmic profiles for tests over rough bottoms (data points between the two "×" markers are used for log-profile fittings): (a) C40_sa (current over the "sandpaper" bottom), (b) SP400a_sa (sinusoidal wave over the "sandpaper" bottom), (c) C40_ce (current over the marble bottom), (d) SP400a_ce (sinusoidal wave over the marble bottom).

Figure 11: Conceptual sketch of near-bottom flow interaction with roughness elements: (a) roughness elements of the "sandpaper" bottom, (b) roughness elements of densely packed sand grains.

Figure 12: Directional dependency of bottom roughness for the ceramic-marble bottom.

Figure 13: First three harmonics of the measured Reynolds-averaged velocity of a sinusoidal wave test SP400a_ce (gray zone indicates standard deviation from spatial averaging): (a) first-harmonic velocity amplitude, (b) first-harmonic velocity phase, (c) second-harmonic velocity amplitude, (d) second-harmonic velocity phase, (e) third-harmonic velocity amplitude, (f) third-harmonic velocity phase.

Figure 14: First two harmonics of the measured Reynolds-averaged velocity: a forward-leaning wave FL320a_ce (solid lines) and a Stokes wave ST400a_ce (dashed lines): (a) dimensionless first-harmonic velocity amplitude, (b) first-harmonic velocity phase, (c) dimensionless second-harmonic velocity amplitude, (d) second-harmonic velocity phase lead.

Figure 15: Dimensionless boundary layer thickness as a function of the inverse relative roughness: (a) the elevation of the maximum first-harmonic amplitude overshoot ζ_m, (b) the elevation ζ_w of 1% complex first-harmonic velocity deficit.

Figure 16: Boundary layer streaming: (a) sinusoidal wave SP400a, (b) forward leaning wave FL320a, (c) Stokes wave ST400a.

Figure 17: Period-averaged vertical velocity profiles of three representative tests (SP400a, ST400a and FL320a) over three bottom conditions: (a) "sandpaper" bottom, (b) ceramic-marble bottom, (c) smooth bottom, (d) smooth bottom with measurement at one-quarter width from the sidewall ((a) to (c) are obtained along the lateral centerline of the test channel).

Figure 18: Conceptual drawing of secondary flows in a straight channel with squared cross-section: (a) smooth bottom, (b) rough bottom.

Figure 19: Instantaneous double-averaged velocity profiles of test SP400a_ce and the associated log-profile fittings over half of the wave period.

Figure 20: Time series of shear velocity obtained from log-profile fittings of test SP400a_ce (circles: modified log-profile fitting with a known bottom roughness scale z_0, crosses: log-profile fittings without a fixed z_0).

Figure 21: Comparison of first-harmonic shear stresses given by momentum integral (solid lines) and Reynolds stress (dots) for sinusoidal wave test SP400a over the three bottom configurations: (a) and (b) smooth bottom, (c) and (d) "sandpaper" bottom, (e) and (f) ceramic-marble bottom.

Figure 22: Comparison of first-harmonic Reynolds stress for test SP400a_sa sampled with two PIV resolution (solid lines: fine resolution: dots: coarse resolution): (a) amplitude, (b) phase.

Figure 23: Bottom shear stress of SP400a_ce (sinusoidal test over the ceramic-marble bottom): (thin solid line: the first harmonic, thin dashed line: the third harmonic, dots: measurements, thick solid line: smoothed time series given by the sum of the first and third harmonics).

Figure 24: Maximum bottom shear stress of sinusoidal wave tests: (a) Wave friction factor, (b) phase lead of the maximum bottom shear stress.

Figure 25: Amplitudes, in terms of the friction factors defined by Eqs. (36) to (38), and phases of the first three harmonics of bottom shear stress for sinusoidal, Stokes, and forward-leaning waves: (a) first-harmonic friction factor, (b) first-harmonic phase lead, (c) second-harmonic friction factor, (d) second-harmonic phase lead, (e) third-harmonic friction factor, (f) second-harmonic phase lead.

Table 1: Target flow conditions (a_1: first-harmonic displacement amplitude of the piston, $U_{\infty,1}$: approximated amplitude of the free-stream first-harmonic velocity, T: wave period, $Re = U_{\infty,1}A_{\infty,1}/\nu$: Reynolds number based on the amplitude of the first-harmonic free-stream velocity and $\nu = 0.8 \cdot 10^{-6} m^2/s$ at a room temperature of 25°C).

Test ID	Wave shape	a_1 $[mm]$	$U_{\infty,1}$ $[cm/s]$	T $[s]$	Re (10^6)
SP400a	Sinusoidal	400	157.9	6.25	3.1
SP400b	Sinusoidal	400	79.0	12.5	1.6
SP250	Sinusoidal	250	98.7	6.25	1.2
SP200	Sinusoidal	200	39.5	12.5	0.4
ST400a	Stokes	400	157.9	6.25	3.1
ST400b	Stokes	400	79.0	12.5	1.6
ST200	Stokes	200	79.0	6.25	0.4
FL320a	Forward-leaning	320	126.3	6.25	2.1
FL320b	Forward-leaning	320	63.2	12.5	1.1
FL160	Forward-leaning	160	63.2	6.25	0.5

Table 2: Assessment of flow generation based on a Stokes wave test (ST400a) over the smooth bottom ($U_{\infty,1}$, $U_{\infty,2}$ and $U_{\infty,3}$: amplitudes of the first three harmonics of free-stream velocity, $\varphi_{\infty,2}$: phase of the second-harmonic free-stream velocity).

	$U_{\infty,1}$ $[cm/s]$	$U_{\infty,2}$ $[cm/s]$	$U_{\infty,3}$ $[cm/s]$	$\varphi_{\infty,2}$ $[^\circ]$
U_{target}	157.91	39.48	0	0
U_{piston}	157.52	39.50	2.41	-5.42
$U_{PIV,1}$	157.06	39.84	2.44	-5.56
$U_{PIV,2}$	157.88	40.39	2.76	-4.92

Table 3: Optimal zero bottom offset Δ ($z = y+\Delta$) and corresponding minimum coefficient of determination (1-R^2) obtained from log-profile fitting

	min(1-R^2)	Δ [mm]
Ceramic-marble bottom		
SP400a_ce	$8.8 \cdot 10^{-5}$	3.6
SP400b_ce	$2.4 \cdot 10^{-5}$	4.7
SP250_ce	$7.0 \cdot 10^{-5}$	3.8
SP200_ce	$1.4 \cdot 10^{-4}$	3.7
C40_ce	$4.3 \cdot 10^{-5}$	3.8
C13_ce	$4.0 \cdot 10^{-5}$	4.3
"sandpaper" bottom		
SP400a_sa	$1.4 \cdot 10^{-5}$	0.45
SP400b_sa	$7.4 \cdot 10^{-5}$	0.63
SP250_sa	$6.0 \cdot 10^{-5}$	0.71
C40_sa	$3.1 \cdot 10^{-5}$	0.66
C45_sa	$2.8 \cdot 10^{-5}$	0.56

Table 4: Results of log-profile fittings for tests over the smooth bottom (1-R^2: coefficient of determination, u_*: fitted shear velocity, $\pm\Delta u_*/u_*$: relative 95% confidence interval of u_*, k_b: fitted bottom roughness, $r_{\Delta k}$: 95% confidence factor of k_b, $k_{b,p}$: bottom roughness predicted using fitted u_*).

Test ID	1-R^2	u_*[cm/s]	$\pm\Delta u_*/u_*$	k_b [mm]	$r_{\Delta k}$	$k_{b,p} = 3.3\nu/u_*$ [mm]	$k_{b,p}/\ k_b$
			Currents				
C13_sm	$4.0 \cdot 10^{-4}$	0.67	1.03%	0.44	1.04	0.39	0.89
C30_sm	$1.9 \cdot 10^{-4}$	1.35	0.61%	0.21	1.03	0.19	0.93
C40_sm	$1.1 \cdot 10^{-4}$	1.74	0.64%	0.14	1.03	0.15	1.05
C45_sm	$4.3 \cdot 10^{-4}$	2.14	1.19%	0.13	1.06	0.12	0.97
			Sinusoidal waves				
SP250_sm	$4.8 \cdot 10^{-5}$	4.91	2.11%	0.062	1.13	0.054	0.87
SP400b_sm	$1.6 \cdot 10^{-4}$	3.85	1.73%	0.086	1.10	0.069	0.80
SP400a_sm	$8.4 \cdot 10^{-4}$	7.28	5.34%	0.045	1.37	0.036	0.81

Table 5: Results of log-profile fittings for tests over the "sandpaper" bottom (1-R^2: coefficient of determination, u_*: fitted shear velocity, $\pm\Delta u_*/u_*$: relative 95% confidence interval of u_*, k_b: fitted bottom roughness, $r_{\Delta k}$: 95% confidence factor of k_b, $Re_* = u_* k_N/\nu$: roughness Reynolds number with k_N=3.7mm).

Test ID	1-R^2	u_* $[cm/s]$	$\Delta u_*/u_*$	k_b $[mm]$	$r_{\Delta k}$	Re_*
			Currents			
C13_sa	$4.4 \cdot 10^{-4}$	0.71	1.59%	0.73	1.14	33
C26_sa	$3.8 \cdot 10^{-5}$	1.35	0.44%	0.88	1.04	62
C40_sa	$7.0 \cdot 10^{-5}$	2.18	0.43%	1.08	1.04	100
C45_sa	$4.5 \cdot 10^{-5}$	2.49	0.34%	1.17	1.03	114
			Sinusoidal waves			
SP200_sa	$1.0 \cdot 10^{-3}$	3.27	5.89%	1.88	1.55	151
SP400b_sa	$7.6 \cdot 10^{-5}$	6.34	0.71%	3.15	1.04	293
SP250_sa	$1.0 \cdot 10^{-4}$	8.93	1.01%	3.77	1.06	411
SP400a_sa	$6.0 \cdot 10^{-5}$	13.25	0.63%	3.60	1.04	611

Table 6: Results of log-profile fittings for tests over the ceramic-marble bottom (1-R^2: coefficient of determination, u_*: fitted shear velocity, $\pm\Delta u_*/u_*$: relative 95% confidence interval of u_*, k_b: fitted bottom roughness, $r_{\Delta k}$: 95% confidence factor of k_b, $Re_* = u_* k_N/\nu$: roughness Reynolds number with k_N=20mm).

Test ID	1-R^2	u_* $[cm/s]$	$\Delta u_*/u_*$	k_b $[mm]$	$r_{\Delta k}$	Re_*
			Currents			
C13_ce	$6.9 \cdot 10^{-5}$	1.15	0.42%	15.7	1.02	287
C40_ce	$6.6 \cdot 10^{-5}$	3.55	0.49%	19.18	1.02	887
			Sinusoidal waves			
SP200_ce	$1.4 \cdot 10^{-4}$	5.38	2.21%	22.03	1.12	1346
SP250_ce	$7.5 \cdot 10^{-5}$	13.19	0.86%	20.77	1.05	3298
SP400b_ce	$9.5 \cdot 10^{-5}$	9.58	0.79%	22.95	1.04	2394
SP400a_ce	$1.2 \cdot 10^{-5}$	17.59	0.88%	16.76	1.05	4398

Table 7: First-harmonic bottom shear stress estimated using the momentum integral method (Integral: numerical integral based on actual measurements, Extrap.: extrapolation term, Total: first-harmonic bottom shear stress given by adding the extrapolation term to the numerical integral)

	Amplitude [cm^2/s^2]			Phase [°]		
	Integral	Extrap.	Total	Integral	Extrap.	Total
SP400a_ce	161.3	53.5	193.2	12.5	76.6	28.7
SP250_ce	66.0	32.6	80.8	1.0	76.2	24.0
SP200_ce	10.0	5.4	12.6	2.7	76	26.7

Table 8: Comparison of first-harmonic bottom shear stresses afforded by the momentum integral method and the log-profile fitting method (MI: the momentum integral method, L: the log-profile fitting method).

	Amplitude [cm^2/s^2]			Phase [°]		
	MI	L	MI/L	MI	L	MI-L
			Smooth bottom			
SP250_sm	19.3	20.3	94.9%	16.1	12.9	3.3
SP400a_sm	49.0	44.4	110.3%	12.6	12.6	0.0
FL320b_sm	8.3	8.8	93.9%	8.5	12.8	-4.3
FL320a_sm	30.3	35.4	85.6%	6.9	11.8	-4.9
FL160_sm	10.5	8.2	128.3%	8.0	11.0	-3.0
ST400a_sm	43.7	47.7	91.5%	6.3	12.4	-6.1
ST200_sm	12.5	13.3	94.1%	13.4	12.7	0.7
ST400b_sm	12.5	12.1	103.6%	2.5	13.8	-11.4
Average			100±14%			-3.2±4.6°
			"Sandpaper" bottom			
SP200_sa	7.1	9.1	78.0%	15.9	19.8	-3.9
SP250_sa	41.9	66.6	62.9%	20.7	19.6	1.1
SP400b_sa	23.1	33.5	69.0%	18.4	19.3	-0.9
SP400a_sa	101.2	145.9	69.3%	19.8	18.1	1.7
FL320b_sa	14.9	20.9	71.6%	23.4	18.9	4.5
FL320a_sa	61.2	103.1	59.4%	22.1	18.4	3.7
FL160_sa	24.9	29.7	83.7%	19.9	19.8	0.1
ST400b_sa	27.2	30.7	88.7%	18.1	20.0	-1.9
ST400a_sa	99.5	147.3	67.5%	22.5	18.2	4.2
ST200_sa	29.5	44.4	66.5%	22.4	21.2	1.2
Average			72±9%			1.0±2.7°
			Ceramic-marble bottom			
SP200_ce	12.6	22.2	57.0%	26.7	24.5	2.2
SP250_ce	80.8	141.1	57.3%	24	22.6	1.4
SP400a_ce	193.2	303.3	63.7%	28.7	23.0	5.7
FL320a_ce	120.8	218.1	55.4%	26.0	19.5	6.5
FL160_ce	38.5	72.7	53.0%	26.4	20.0	6.4
ST400a_ce	201.3	299.9	67.1%	26.5	23.1	3.4
ST200_ce	52.7	102.7	51.3%	26.5	22.7	3.8
Average			58±6%			4.2±2.0°

Figure 1:

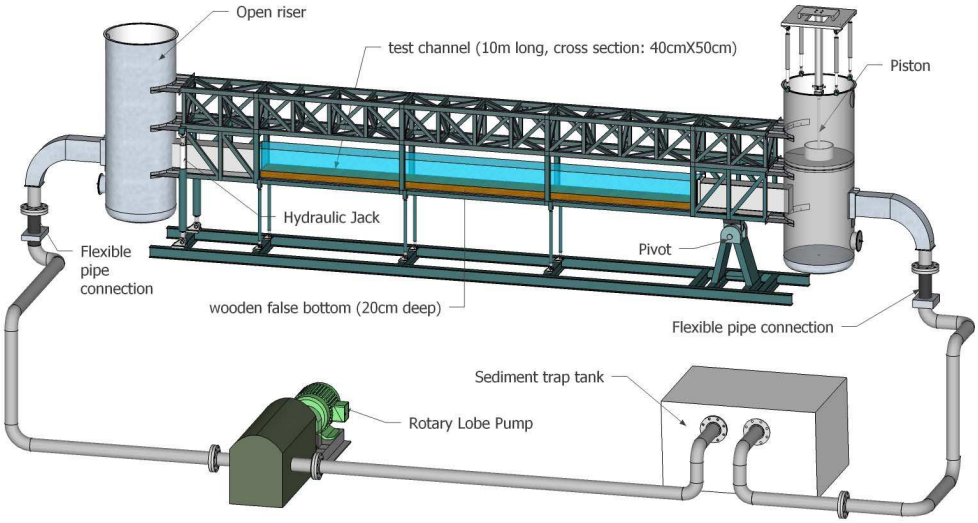
Open riser
test channel (10m long, cross section: 40cmX50cm)
Piston
Hydraulic Jack
Flexible pipe connection
Pivot
wooden false bottom (20cm deep)
Flexible pipe connection
Sediment trap tank
Rotary Lobe Pump

Figure 2:

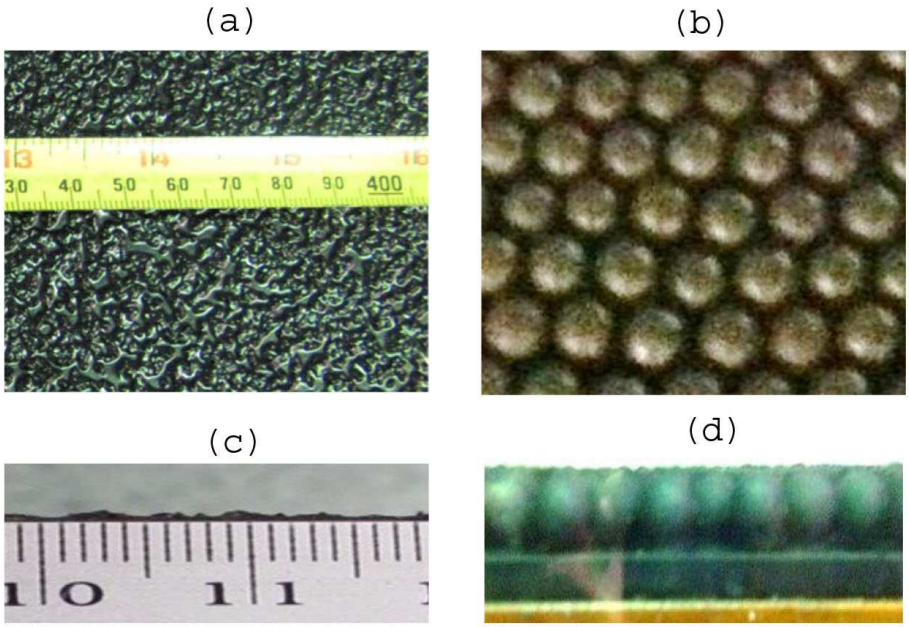

Figure 3:

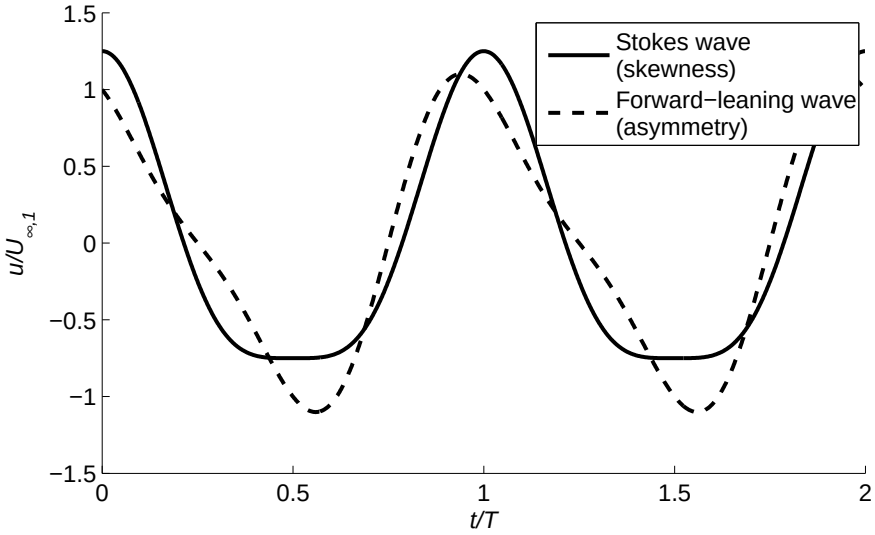
Stokes wave
(skewness)
Forward−leaning wave
(asymmetry)
u/U∞,1
t/T
1.5
1
0.5
0
−0.5
−1
−1.5
0
0.5
1
1.5
2

Figure 4:

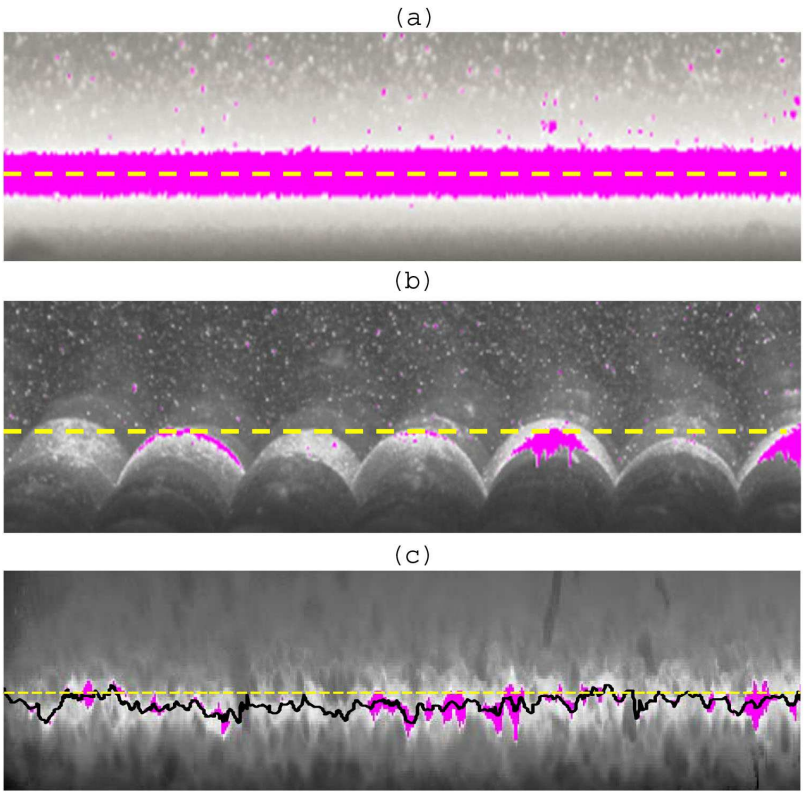

Figure 5:

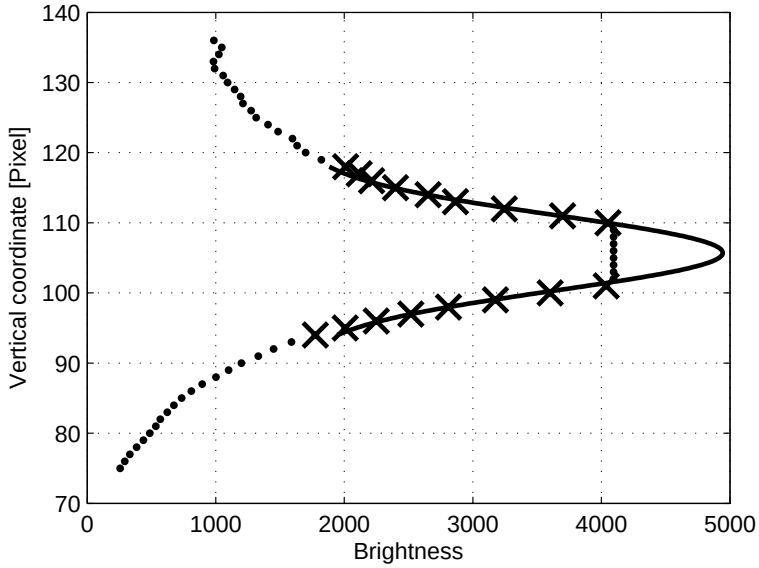
140
130
120
110
100
90
80
70
0
1000
2000
3000
4000
5000
Vertical coordinate [Pixel]
Brightness

Figure 6:

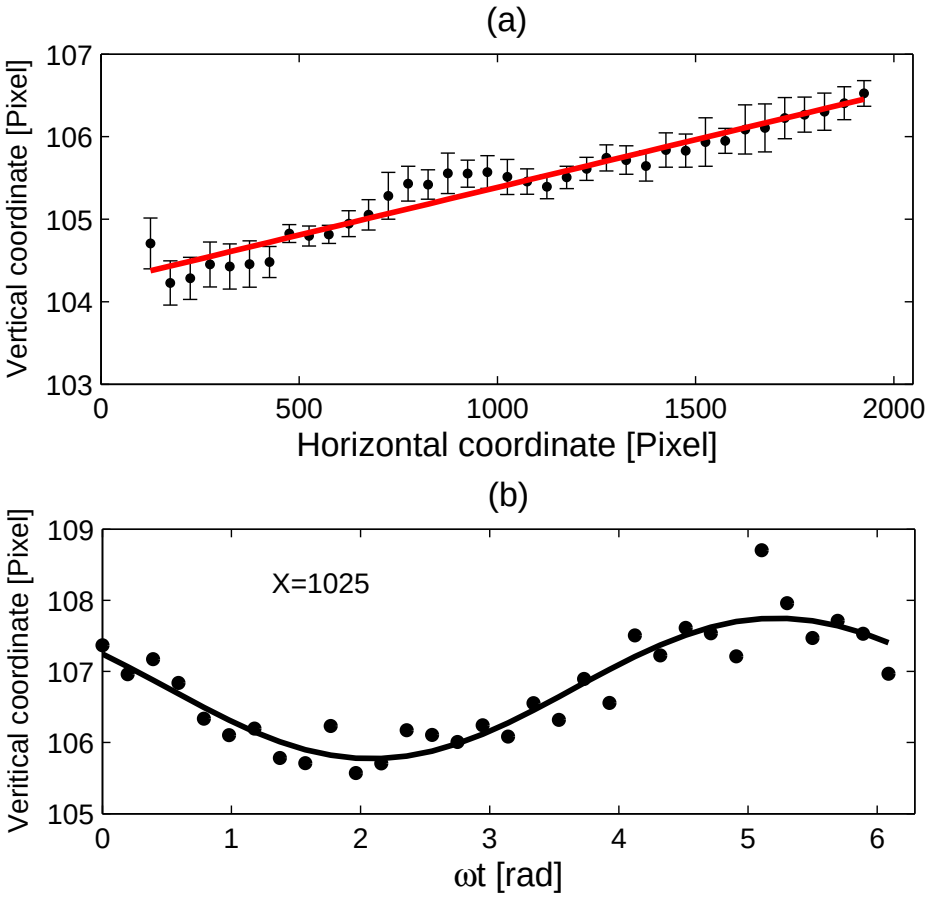
(a)
Vertical coordinate [Pixel]
107
106
105
104
103
0
500
1000
1500
2000
Horizontal coordinate [Pixel]
(b)
Veritical coordinate [Pixel]
109
108
107
106
105
X=1025
0
1
2
3
4
5
6
ωt [rad]

Figure 7:

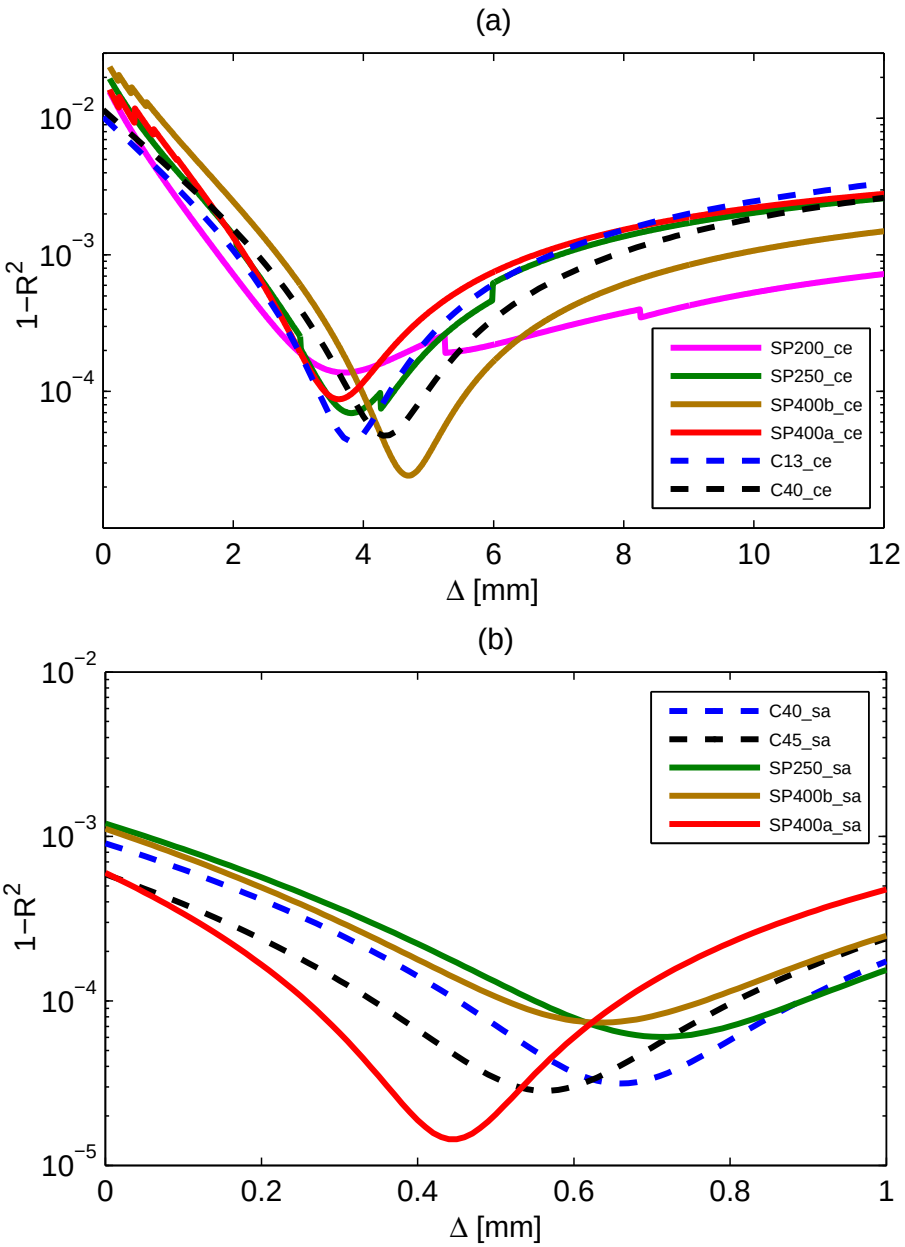
(a)
10^{-2}
10^{-3}
10^{-4}
$1-R^2$
0
2
4
6
8
10
12
Δ [mm]
SP200_ce
SP250_ce
SP400b_ce
SP400a_ce
C13_ce
C40_ce
(b)
10^{-2}
10^{-3}
10^{-4}
10^{-5}
$1-R^2$
0
0.2
0.4
0.6
0.8
1
Δ [mm]
C40_sa
C45_sa
SP250_sa
SP400b_sa
SP400a_sa

Figure 8:

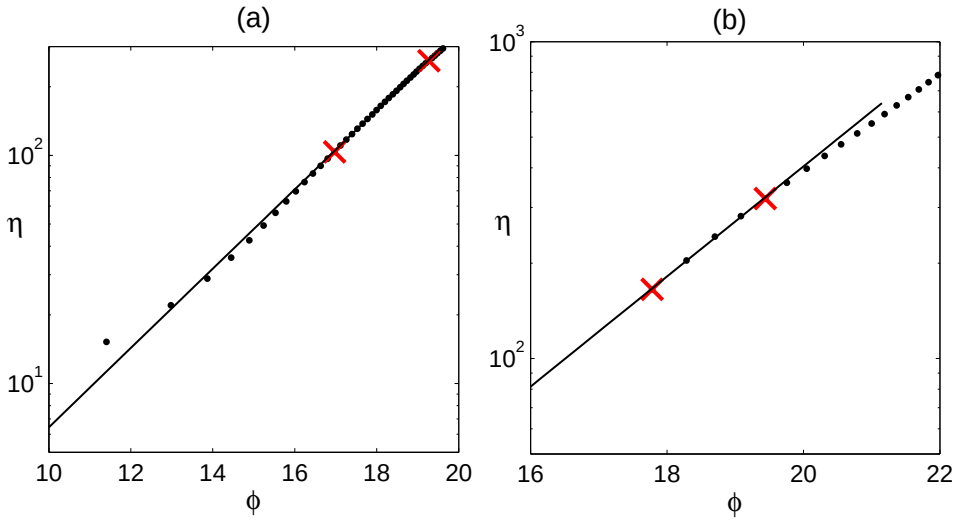

Figure 9:

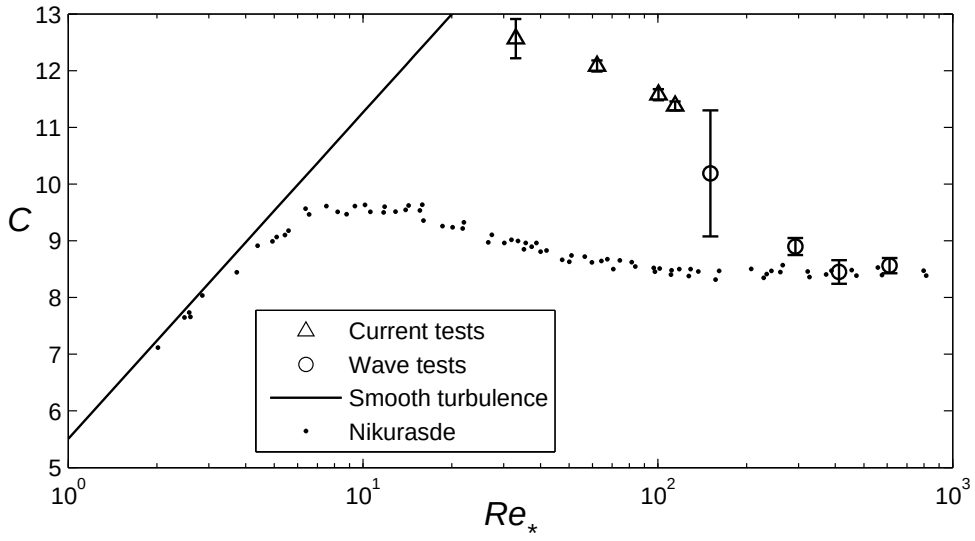
13
12
11
10
9
8
7
6
5
C
10^0
10^1
10^2
10^3
Re_*
Current tests
Wave tests
Smooth turbulence
Nikurasde

Figure 10:

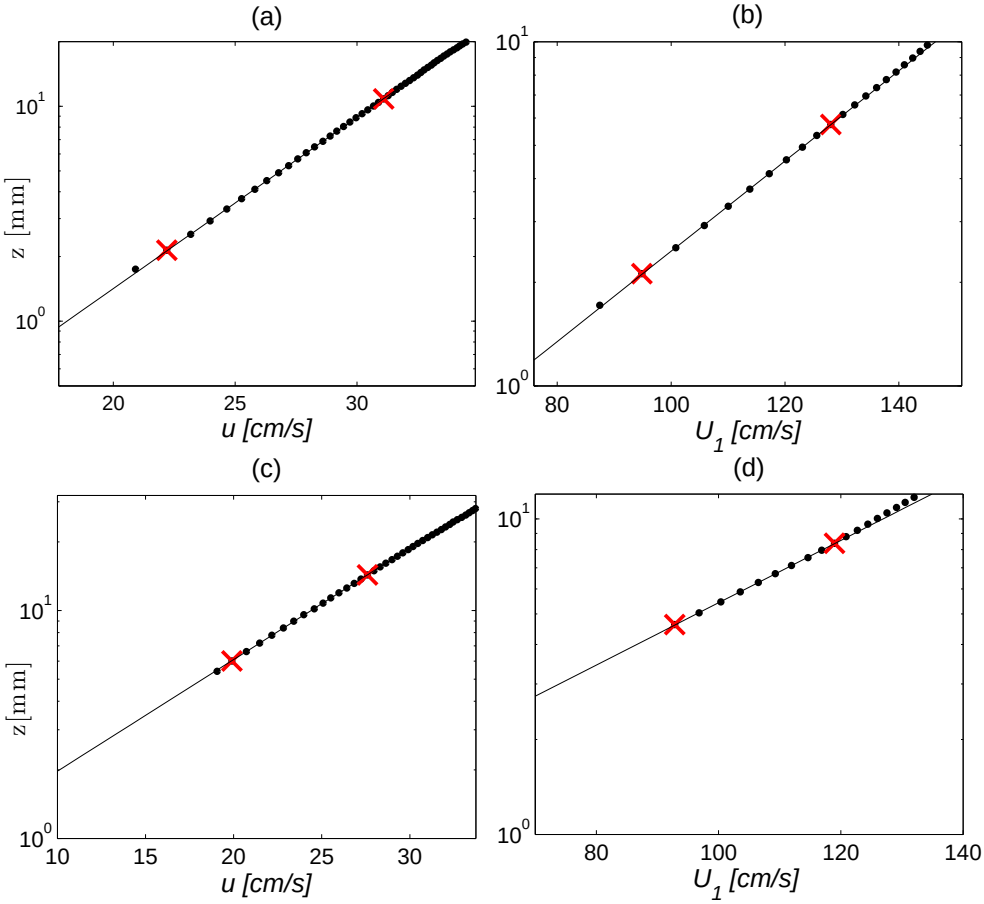

Figure 11:

(a)

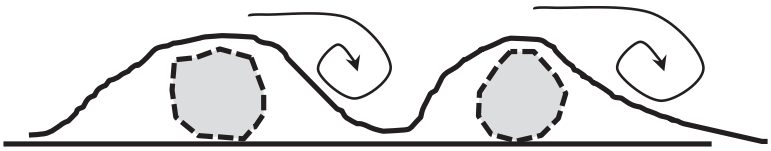

(b)

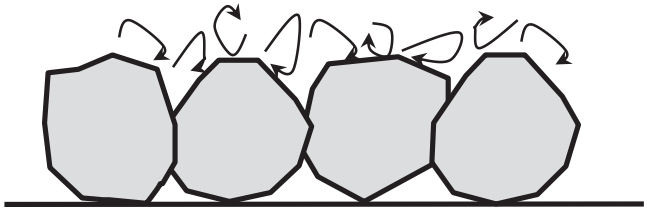

Figure 12:

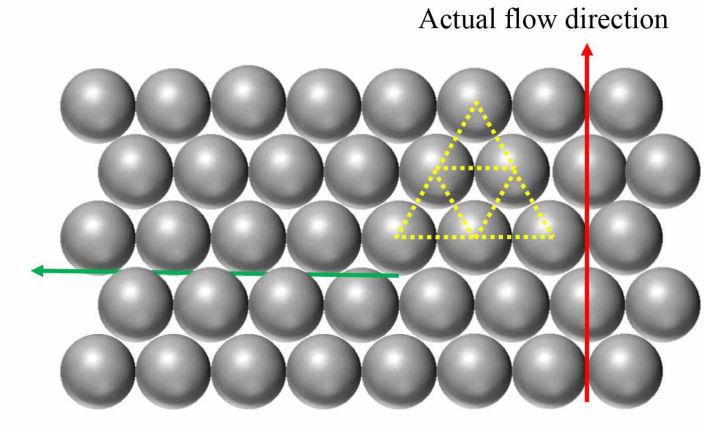

Figure 13:

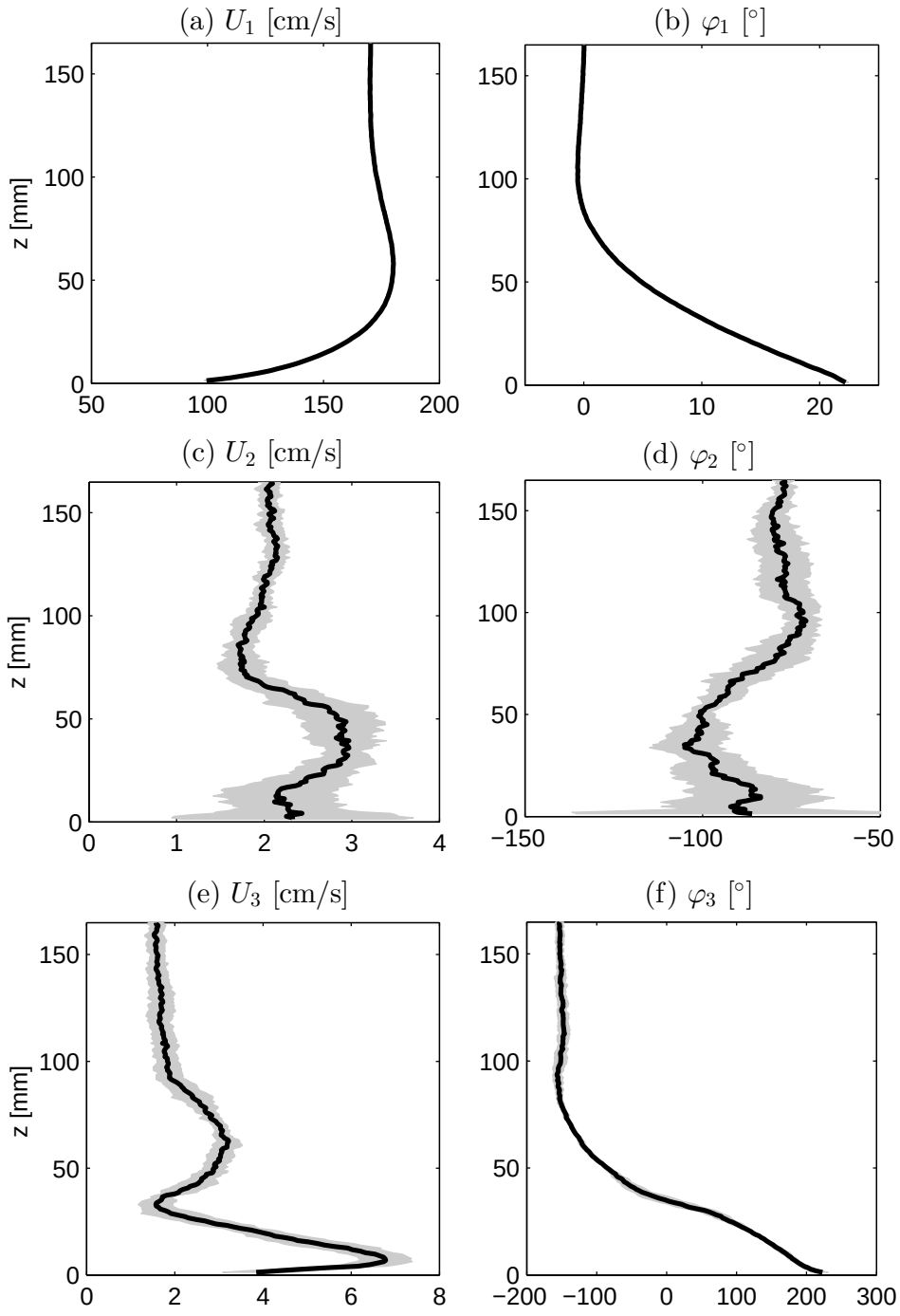
(a) U_1 [cm/s]
(b) φ_1 [°]
(c) U_2 [cm/s]
(d) φ_2 [°]
(e) U_3 [cm/s]
(f) φ_3 [°]
z [mm]
0
50
100
150
200
−150
−100
−50
−200
300

Figure 14:

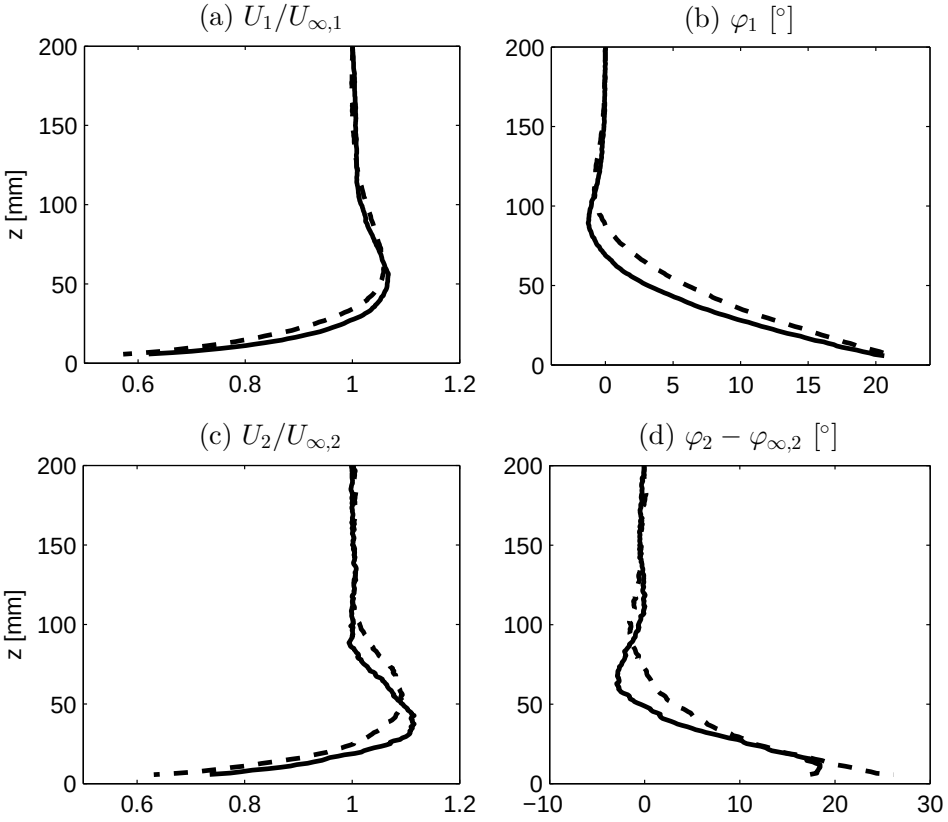
(a) $U_1/U_{\infty,1}$
(b) φ_1 [°]
(c) $U_2/U_{\infty,2}$
(d) $\varphi_2 - \varphi_{\infty,2}$ [°]
z [mm]
z [mm]
200
150
100
50
0
0.6
0.8
1
1.2
0
5
10
15
20
−10
30

Figure 15:

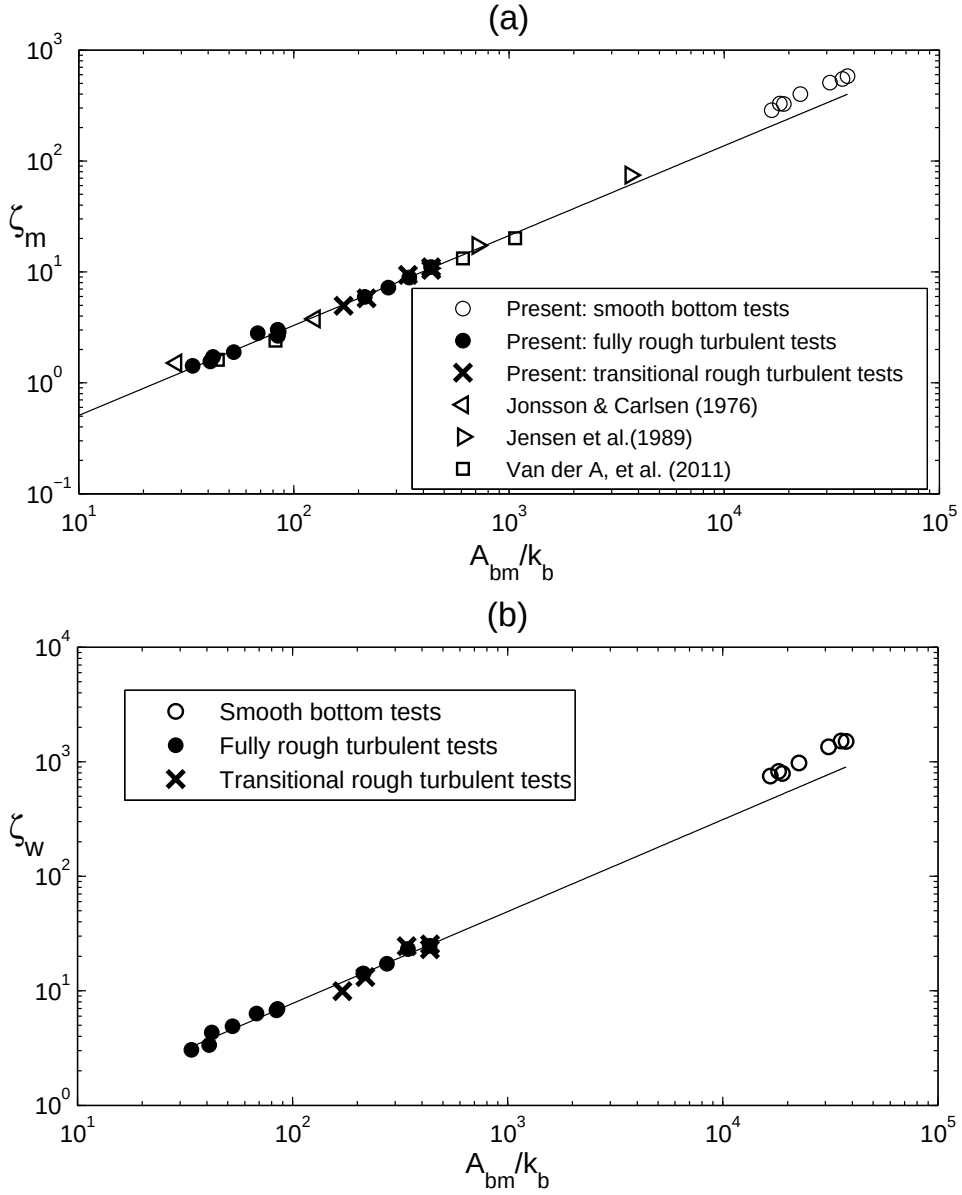
(a)
10^3
10^2
10^1
10^0
10^{-1}
ζ_m
10^1
10^2
10^3
10^4
10^5
A_{bm}/k_b
Present: smooth bottom tests
Present: fully rough turbulent tests
Present: transitional rough turbulent tests
Jonsson & Carlsen (1976)
Jensen et al.(1989)
Van der A, et al. (2011)
(b)
10^4
10^3
10^2
10^1
10^0
ζ_w
10^1
10^2
10^3
10^4
10^5
A_{bm}/k_b
Smooth bottom tests
Fully rough turbulent tests
Transitional rough turbulent tests

Figure 16:

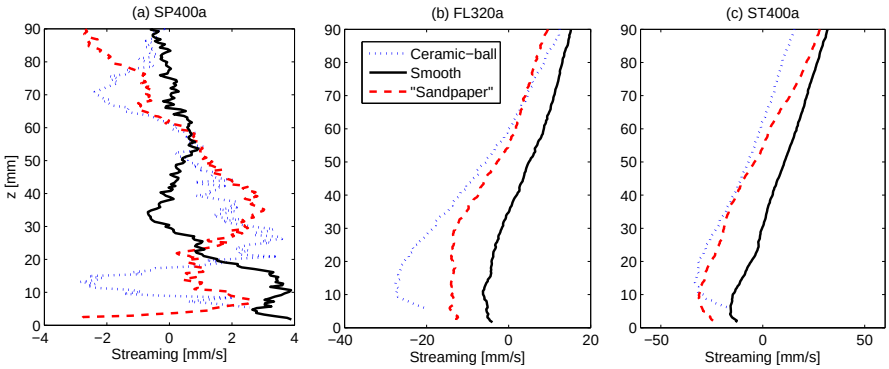
(a) SP400a
(b) FL320a
(c) ST400a
Ceramic−ball
Smooth
"Sandpaper"
z [mm]
Streaming [mm/s]
Streaming [mm/s]
Streaming [mm/s]

Figure 17:

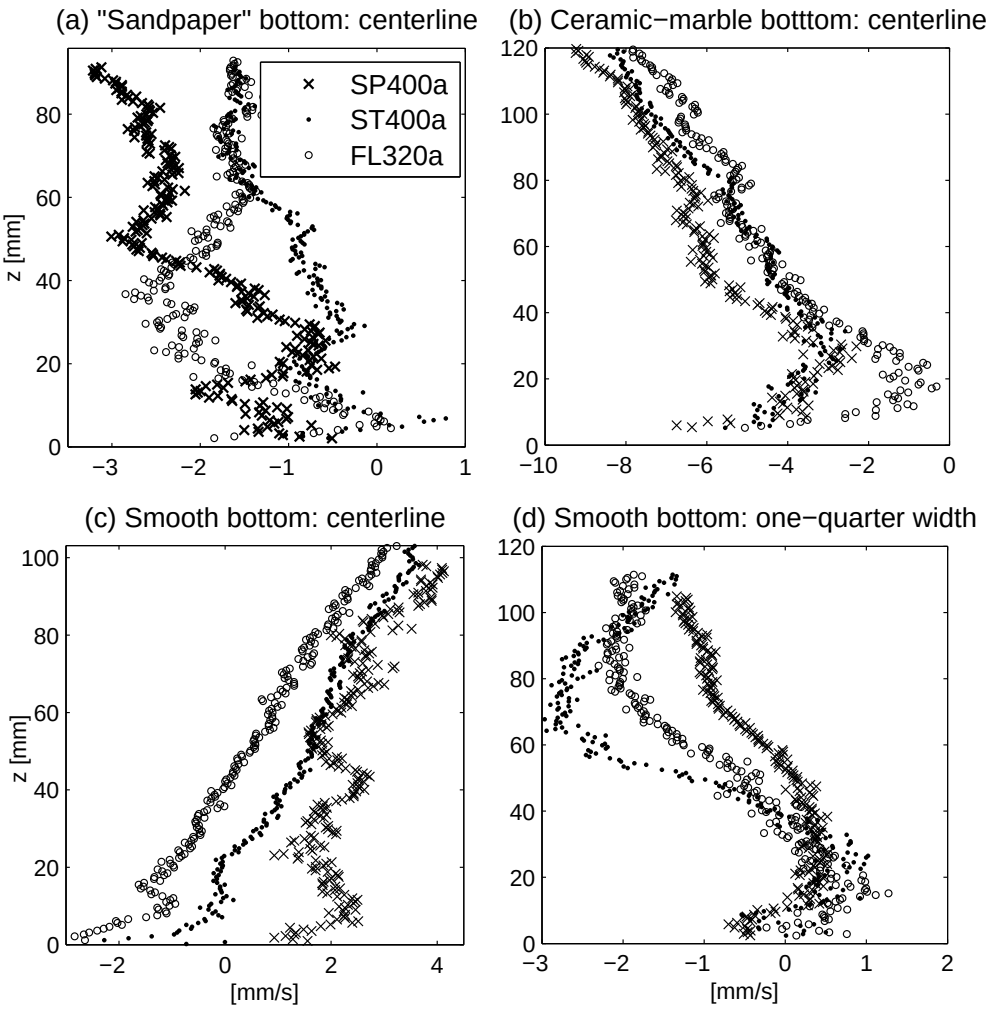
(a) "Sandpaper" bottom: centerline
(b) Ceramic−marble botttom: centerline
(c) Smooth bottom: centerline
(d) Smooth bottom: one−quarter width
SP400a
ST400a
FL320a
z [mm]
[mm/s]

Figure 18:

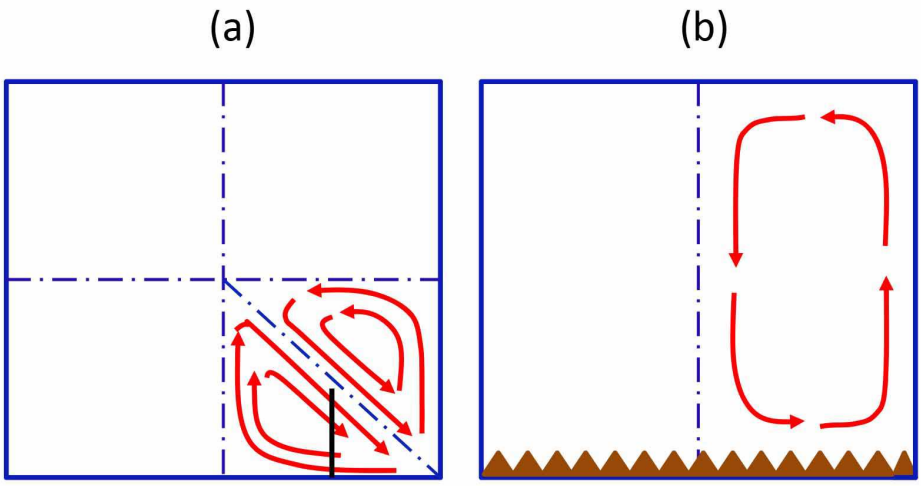

Figure 19:

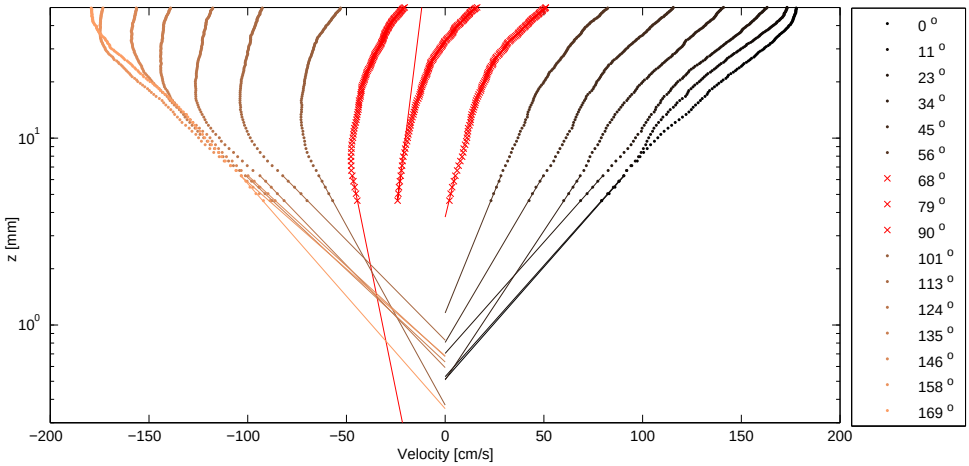
z [mm]
Velocity [cm/s]
0 o
11 o
23 o
34 o
45 o
56 o
68 o
79 o
90 o
101 o
113 o
124 o
135 o
146 o
158 o
169 o

Figure 20:

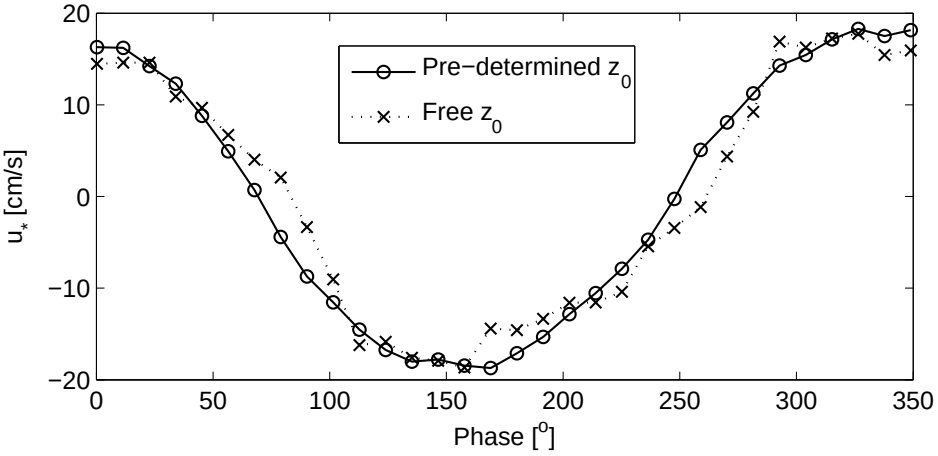
Pre−determined z0
Free z0
u* [cm/s]
Phase [o]
20
10
0
−10
−20
0
50
100
150
200
250
300
350

Figure 21:

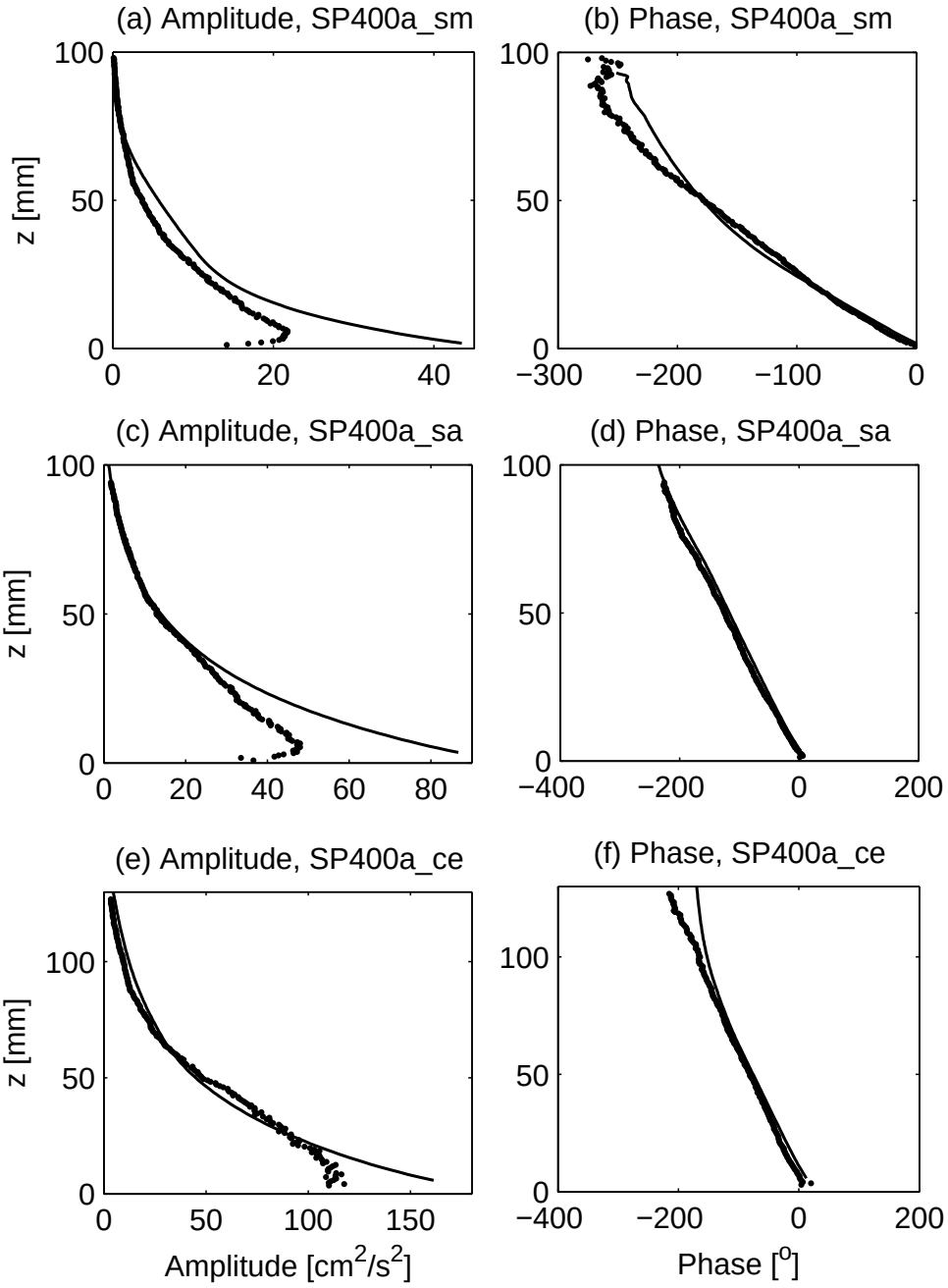
(a) Amplitude, SP400a_sm
(b) Phase, SP400a_sm
(c) Amplitude, SP400a_sa
(d) Phase, SP400a_sa
(e) Amplitude, SP400a_ce
(f) Phase, SP400a_ce
z [mm]
Amplitude [cm^2/s^2]
Phase [^{o}]

Figure 22:

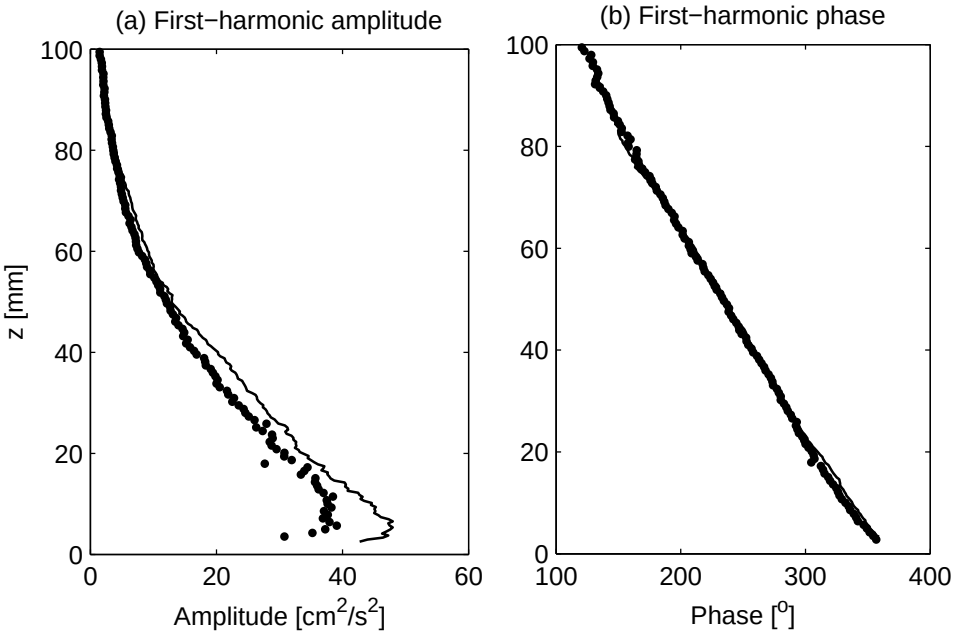
(a) First−harmonic amplitude
(b) First−harmonic phase
z [mm]
Amplitude [cm^2/s^2]
Phase [^{o}]
0
20
40
60
80
100
0
20
40
60
100
200
300
400

Figure 23:

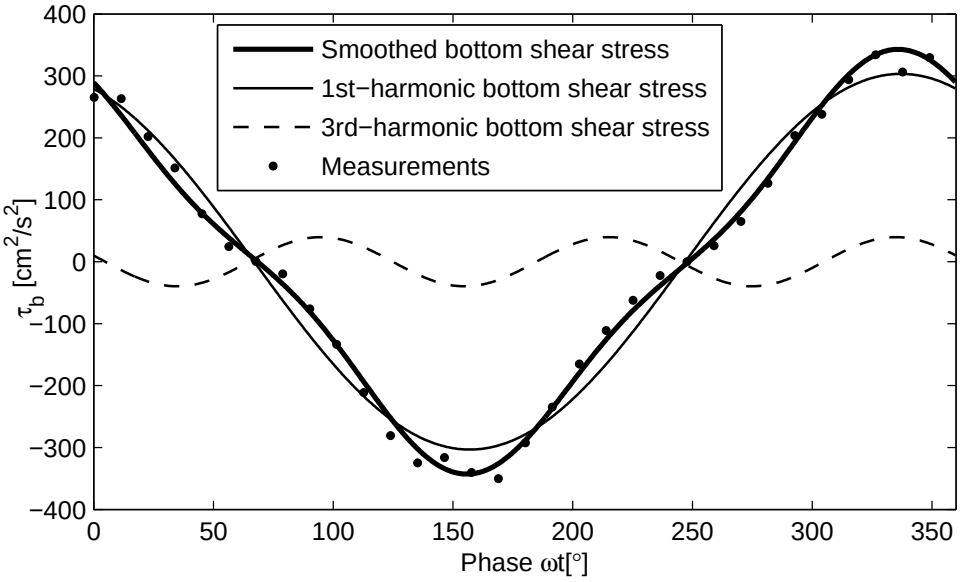
Smoothed bottom shear stress
1st−harmonic bottom shear stress
3rd−harmonic bottom shear stress
Measurements
τb [cm2/s2]
Phase ωt[°]
400
300
200
100
0
−100
−200
−300
−400
0
50
100
150
200
250
300
350

Figure 24:

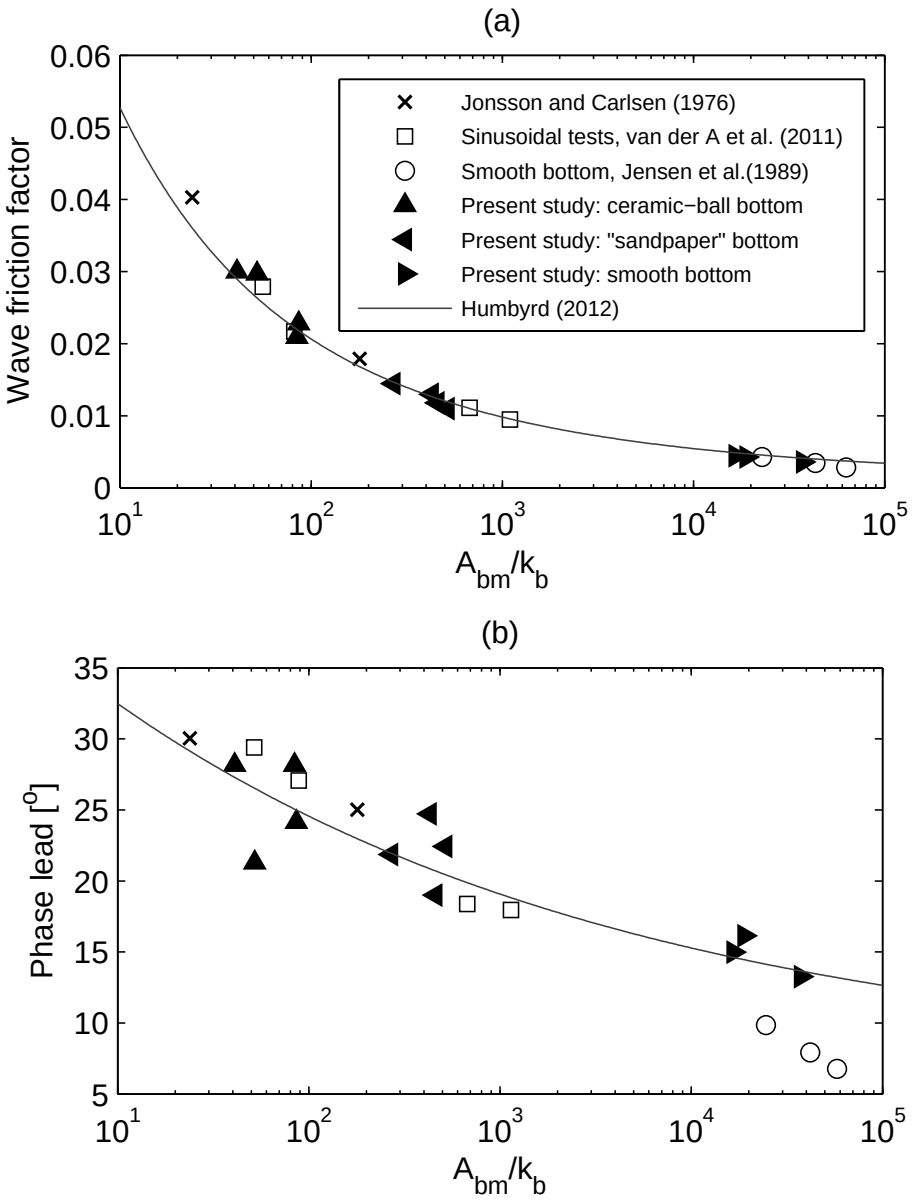
(a)
Wave friction factor
0.06
0.05
0.04
0.03
0.02
0.01
0
10^1
10^2
10^3
10^4
10^5
A_{bm}/k_b
Jonsson and Carlsen (1976)
Sinusoidal tests, van der A et al. (2011)
Smooth bottom, Jensen et al.(1989)
Present study: ceramic−ball bottom
Present study: "sandpaper" bottom
Present study: smooth bottom
Humbyrd (2012)
(b)
Phase lead [^{o}]
35
30
25
20
15
10
5
10^1
10^2
10^3
10^4
10^5
A_{bm}/k_b

Figure 25:

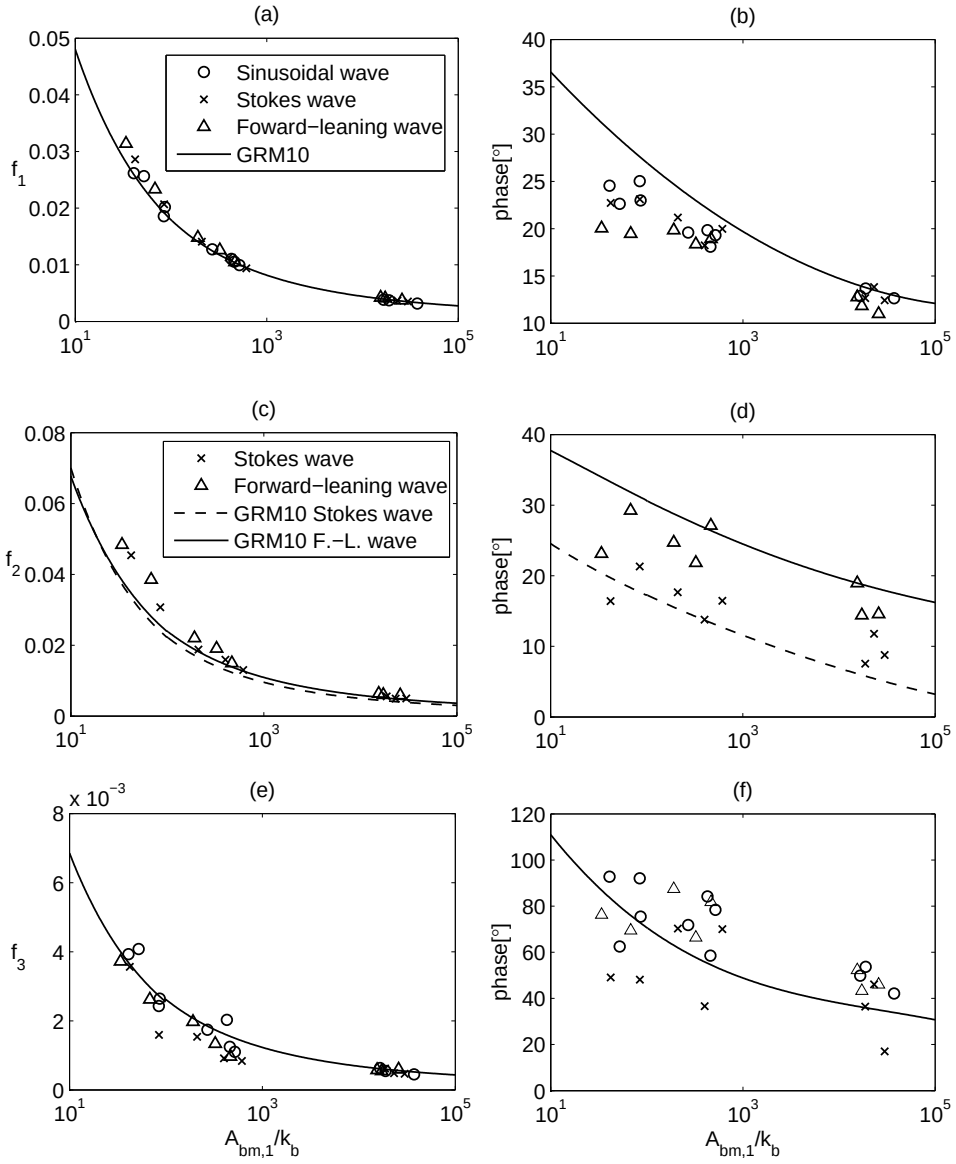
(a)
(b)
(c)
(d)
(e)
(f)
Sinusoidal wave
Stokes wave
Foward−leaning wave
GRM10
Stokes wave
Forward−leaning wave
GRM10 Stokes wave
GRM10 F.−L. wave
f1
f2
f3
phase[°]
x 10−3
Abm,1/kb